

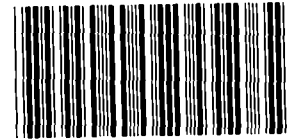
SANDIA REPORT

SAND93-0027 • UC-410

Unlimited Release

Printed February 1993

MICROFICHE

Multiphase Equation of State for Iron

8562383

SANDIA NATIONAL
LABORATORIES
TECHNICAL LIBRARY

Gerald I. Kerley

Prepared by
Sandia National Laboratories
Albuquerque, New Mexico 87185 and Livermore, California 94550
for the United States Department of Energy
under Contract DE-AC04-76DP00789

J. J. Reilly

Issued by Sandia National Laboratories, operated for the United States Department of Energy by Sandia Corporation.

NOTICE: This report was prepared as an account of work sponsored by an agency of the United States Government. Neither the United States Government nor any agency thereof, nor any of their employees, nor any of their contractors, subcontractors, or their employees, makes any warranty, express or implied, or assumes any legal liability or responsibility for the accuracy, completeness, or usefulness of any information, apparatus, product, or process disclosed, or represents that its use would not infringe privately owned rights. Reference herein to any specific commercial product, process, or service by trade name, trademark, manufacturer, or otherwise, does not necessarily constitute or imply its endorsement, recommendation, or favoring by the United States Government, any agency thereof or any of their contractors or subcontractors. The views and opinions expressed herein do not necessarily state or reflect those of the United States Government, any agency thereof or any of their contractors.

Printed in the United States of America. This report has been reproduced directly from the best available copy.

Available to DOE and DOE contractors from
Office of Scientific and Technical Information
PO Box 62
Oak Ridge, TN 37831

Prices available from (615) 576-8401, FTS 626-8401

Available to the public from
National Technical Information Service
US Department of Commerce
5285 Port Royal Rd
Springfield, VA 22161

NTIS price codes
Printed copy: A04
Microfiche copy: A01

Multiphase Equation of State for Iron

Gerald I. Kerley
Computational Physics and Mechanics Department
Sandia National Laboratories
Albuquerque, NM 87185

Abstract

The PANDA code is used to build a multiphase equation of state (EOS) table for iron. Separate EOS tables were first constructed for each of the individual phases. The phase diagram and multiphase EOS were then determined from the Helmholtz free energies. The model includes four solid phases (α , γ , δ , and ϵ) and a fluid phase (including the liquid, vapor, and supercritical regions). The model gives good agreement with experimental thermophysical data, static compression data, phase boundaries, and shock-wave measurements. Contributions from thermal electronic excitation, computed from a quantum-statistical-mechanical model, were found to be very important. This EOS covers a wide range of densities (0 - 1000 g/cm³) and temperatures (0 - 1.2×10⁷K). It is also applicable to RHA steel. The new EOS is used in hydrocode simulations of plate impact experiments, a nylon ball impact on steel, and the shaped charge perforation of an RHA plate. The new EOS table can be accessed through the SNL-SESAME library as material number 2150.

Acknowledgment

An improved equation of state (EOS) for iron, one that includes a realistic treatment of its interesting phase diagram, is long overdue. This work was undertaken after a survey of various CTH users indicated that the highest priority for new EOS should be assigned to iron and RHA steel. I am grateful to Gene Hertel for conducting this survey, to those who participated in it, and to DARPA for funding. I also thank Paul Yarrington for his support and encouragement, and Charlie Anderson, for sending me the shock data for RHA.

As always, I thank my wife Donna, whose love, prayers, and encouragement are what keep me going.

Contents

Acknowledgment	4
Contents	5
Figures	6
Tables	6
Symbols and Units	7
1. Introduction	8
2. Description of the Model	10
2.1 Solid Phases	10
2.2 Fluid Phases	12
2.3 Thermal Electronic Contributions	13
2.4 Multiphase EOS Calculations	15
3. Results and Discussion	16
3.1 Thermophysical Data	16
3.2 Static Compression Data	16
3.3 Phase Diagram	18
3.4 Melting	19
3.5 Shock-Wave Behavior	19
3.6 RHA Steel	21
4. Hydrocode Calculations	23
4.1 Wave-Profile Measurements	23
4.2 Nylon Ball Impact on Iron	24
4.3 Shaped Charge Perforation of RHA Steel	26
5. Conclusions	29
References	30
Appendix A: Calculation of Thermal Electronic Entropy Table	34
Appendix B: Output File for Multiphase EOS Calculation	36
Distribution	46

Figures

Fig. 1. Electronic contribution to the entropy for iron.....	14
Fig. 2. Electronic contribution to the pressure for iron.....	14
Fig. 3. Entropy vs. temperature for iron (zero pressure)	17
Fig. 4. Density vs. temperature for iron (zero pressure).....	17
Fig. 5. Comparison of calculated room temperature isotherm with diamond cell measurements	18
Fig. 6. Phase diagram for iron	19
Fig. 7. Shock-induced phase transitions in iron.....	20
Fig. 8. Hugoniot for iron at various initial densities	20
Fig. 9. Hugoniot data for iron and RHA steel.....	22
Fig. 10. Calculated free surface velocities for symmetric impacts of iron plates.....	23
Fig. 11. Calculated velocity at sapphire window for test number 15 of Ref. [42]	24
Fig. 12. CTH calculations of nylon ball impacting steel plate	25
Fig. 13. Sensitivity of nylon-steel impact problem to EOS and material strength	26
Fig. 14. CTH calculations of perforation of RHA plate by shaped charge jet.....	27
Fig. 15. Sensitivity of RHA perforation problem to EOS	28

Tables

Table 1. EOS Constants for Solid Models

Symbols and Units

ρ	density [g/cm^3]
V	specific volume, $V = 1/\rho$ [cm^3/g]
T	temperature [K]
P	pressure [GPa]
E	specific internal energy [MJ/kg]
A	Helmholtz free energy [MJ/kg]
S	entropy [$MJ/(kg \cdot K)$]
C_V	constant volume specific heat, $C_V = (\partial E / \partial T)_V$ [$MJ/(kg \cdot K)$]
β	isothermal bulk modulus, $\beta = \rho (\partial P / \partial \rho)_T$ [GPa]
Γ	Grüneisen function [unitless]
Θ	Debye temperature [K]
$\phi(\mathbf{x}_s)$	atomic potential function (\mathbf{x}_s are coordinates of neighbors)
c_s	sound velocity [km/s]
u_s	shock velocity [km/s]
u_p	particle velocity [km/s]

1. Introduction

The equation of state (EOS) of iron has long been a topic of considerable interest, and there is now a vast literature devoted to it [1] - [5]. This fact is hardly surprising, in view of the importance of iron and its alloys as structural materials. However, much work has also been motivated by interest in modeling the earth's core [4], a problem requiring an understanding of the properties of iron at high temperatures and pressures (3000-7000K, 200-400 GPa). The present work was undertaken to provide an improved EOS for use in armor penetration studies and other impact problems at low, intermediate, and high velocities. Finally, the complexities of the phase diagram and other intriguing properties of iron make it a leading candidate for basic research studies.

Four solid phases of iron have been observed [6]. The alpha phase, which is stable at ambient pressure and temperature, has a bcc structure and exhibits well-known magnetic properties up to the Curie temperature of 1042K [7]. Iron transforms to the gamma phase, which has an fcc structure, at temperatures above 1184K (and zero pressure) [7]. It transforms back to the bcc structure (sometimes called the delta phase) at 1665K before melting at 1809K [7]. The epsilon phase, which was first discovered in shock wave experiments [2], has an hcp structure and is produced at pressures above about 11 GPa [5]. The boiling point of iron is 3135K [7]. The properties and boundaries of the various phases as functions of pressure and temperature have been studied experimentally, using both static and dynamic methods.

In this work, we have used the Panda code [8], which provides the tools needed to model materials having complicated phase diagrams. For example, we have successfully used this method to model the properties of calcium carbonate minerals [9]. Our application of the technique to iron can be summarized as follows:

- Individual tables of thermodynamic properties were constructed for the α , γ , and ϵ phases by combining contributions from the 0K isotherm, lattice vibrations, and thermal electronic excitations. In addition, a magnetic contribution was included for the α -phase.
- A table of the thermodynamic properties for the fluid phase was constructed using fluid perturbation theory [10] to treat the atomic motions, together with the thermal electronic term. The fluid EOS describes not only the liquid, but also the vapor and supercritical regimes.
- Experimental data were used to determine the model parameters wherever possible. The thermal electronic term, which was calculated from an *a priori* model, was found to have a surprisingly large effect upon the thermal expansion of iron as well as its heat capacity.
- A multiphase EOS table was constructed from the EOS tables for the individual phases, assuming thermodynamic equilibrium. Hence, the phase boundaries

were determined by finding the phase having the lowest Gibbs free energy at a given pressure and temperature.

- The multiphase EOS can be used by hydrodynamics codes that have the capability to read the SESAME tabular format, as described in Refs. [11] and [12]. In this way, one can make use of detailed and sophisticated features that could not be included in any analytic EOS model.

The theoretical model is described in Sec. 2 and Appendix A. The Panda output file generated during the multiphase EOS calculation is given in Appendix B. In Sec. 3, we discuss the results of the model and compare them with experimental measurements of thermophysical properties, static compression curves, the phase diagram, and shock wave behavior. In Sec. 4, we discuss hydrocode calculations, made using the CTH code and our new EOS table, of plate impact tests, of the impact of a nylon ball on a steel plate, and of the shaped charge perforation of an RHA plate.

2. Description of the Model

2.1 Solid Phases

The thermodynamic functions for the α , γ , and ϵ phases are assumed to have the following form:

$$P(\rho, T) = P_c(\rho) + P_l(\rho, T) + P_m(\rho, T) + P_e(\rho, T), \quad (1)$$

$$E(\rho, T) = E_c(\rho) + E_l(\rho, T) + E_m(\rho, T) + E_e(\rho, T) - \Delta E_b, \quad (2)$$

and

$$A(\rho, T) = E_c(\rho) + A_l(\rho, T) + A_m(\rho, T) + A_e(\rho, T) - \Delta E_b. \quad (3)$$

Here the subscripts c , l , m , and e denote contributions from the zero-Kelvin curve, lattice vibrations (including the zero-point term), magnetic excitations (α -phase only), and thermal electronic excitations, respectively. ΔE_b is the cohesive energy, which is subtracted in order to give a consistent energy zero for all three phases; values for this constant [13], corrected for the zero-point lattice energy [8], are given in Table 1.

Modern static pressure devices have been used to measure the compression curves for the α and ϵ phases at room temperature [14] - [18] and also at temperatures up to 723K [17]. These various sets of data were corrected to 0K, by subtracting off the calculated thermal pressure corrections P_l and P_e , and fit to the Birch-Murnaghan equation [19],

$$P_c(\rho) = \frac{3}{2}\beta_0(\eta^{7/3} - \eta^{5/3}) \left[1 + \frac{3}{4}(\eta^{2/3} - 1)(\beta'_0 - 4) \right], \quad (4)$$

where $\eta = \rho/\rho_0$, and ρ_0 , β_0 , and β'_0 are constants, given in Table 1. For the γ -phase, the value of ρ_0 was fixed by fitting the thermal expansion data, and β_0 and β'_0 were taken to be intermediate between values for the α and ϵ phases. The γ -phase parameters are also constrained somewhat by the shock data for porous iron. The zero-Kelvin curves were input to Panda using the tabular cold curve option [8], which computes a thermodynamically consistent energy E_c . To insure correct asymptotic behavior at high densities, an extrapolation formula based on Thomas-Fermi theory [8] was used for $\rho > 11.0 \text{ g/cm}^3$ (i.e. $P_c > 100 \text{ GPa}$).

The contributions from lattice vibrations were calculated using the Debye model with a cutoff in the sum over the levels, as implemented in Panda [8]. Input to this model includes the Debye temperature Θ_{ref} and Grüneisen parameter Γ_{ref} at the room temperature solid density ρ_{ref} , and a constant τ , which specifies the density dependence of the Grüneisen function,

$$\Gamma(\rho) = (\Gamma_{ref} - 0.5) (\rho_{ref}/\rho)^\tau - 0.5. \quad (5)$$

Values of Θ_{ref} for the α and γ phases were determined by fitting the model to heat capacity data [7]. Θ_{ref} for the ϵ -phase was taken from Stepakoff and Kaufman [20], who estimated it from the heat capacity of ϵ -stabilized Ru alloys. Values of Γ_{ref} for the α and γ phases were determined from thermal expansion data [6] [21]. Γ_{ref} for the ϵ -phase was chosen by fitting the model to the high temperature PVT data of Huang, et. al. [17]. The “typical” value $\tau = 1$ was used for the α and γ phases, but it was found that better results for the γ - ϵ phase boundary were obtained by making Γ for the ϵ -phase fall off more rapidly with density. Since the ϵ -phase has such a high value for Γ_{ref} , $\tau = 2$ also gives a value of Γ comparable to that for the other two phases at high densities.

TABLE 1: EOS Constants for Solid Models

parameter	α -phase	γ -phase	ϵ -phase
ΔE_b	7.397	7.337	7.397
$\rho_0, \text{g/cm}^3$	7.969	8.060	8.430
β_0, GPa	173.0	174.0	182.0
β'_0	4.80	4.70	5.00
Θ_{ref}, K	425.0	300.0	385.0
Γ_{ref}	1.70	1.65	2.40
ρ_{ref}	7.873	7.953	8.264
τ	1.0	1.0	2.0
$k, \text{MJ/kg/K}^{2.5}$	1.36×10^{-6}	-	-
T_0, K	1080.0	-	-

The magnetic term, included only for the α -phase, was treated in a manner similar to that used by Andrews [1]. He noted that, since the Curie temperature is nearly independent of pressure, it is a good approximation to take the magnetic term as independent of density. As a result, the magnetic term makes no contribution to the pressure ($P_m = 0$). He used the following empirical formula to represent the magnetic contribution to the heat capacity below the Curie temperature:

$$C_{Vm}(T) = kT^{1.5}/(T_0 - T), \quad (6)$$

where the constants k and T_0 , together with other model parameters, were adjusted to match experimental data. Our values for these constants differ from those used by Andrews, because our model for the thermal electronic term predicts larger contributions than his. For the same reason, we simply set $C_{Vm} = 0$ above the Curie point, where Andrews used an expression that approaches zero at high temperatures. Equation (6) was integrated numerically to obtain the energy and free energy and input to Panda using the tabular option [8].

The thermal electronic term is discussed in Sec. 2.3.

2.2 Fluid Phases

The thermodynamic functions for the fluid phases (liquid, vapor, and supercritical fluid) are computed using a version of liquid perturbation theory called the CRIS model [10]. Since this model has been discussed in detail in previous work, we will discuss only a few points here. The Helmholtz free energy is given by

$$A(\rho, T) = A_\phi(\rho, T) + A_e(\rho, T) - \Delta E_b. \quad (7)$$

Here A_ϕ includes both the contributions from electronic binding, in the ground state configuration, and the thermal atomic motion in the force field created by the electrons. (It corresponds to $E_c + A_l$ in Eq. (3), but these two terms are not additive as they are in the solid model.) A_e is the contribution from thermal electronic excitations; the same model is used for the solid and fluid phases and is discussed in Sec. 2.3. ΔE_b is the cohesive energy, which is subtracted to give the same energy zero as for the solid phases. The other thermodynamic quantities are computed from standard thermodynamic relations [8] [10].

In order to compute the properties of a fluid, it is necessary to know something about the function ϕ , which we define as the potential energy of an atom in the field of neighboring atoms. This function, which is determined by the intermolecular forces, is related to the energy of the solid on the zero-Kelvin isotherm by

$$E_c(\rho) = (N_0/W) \phi(\mathbf{x}_s), \quad (8)$$

where N_0 is Avogadro's number, W is the atomic weight, and \mathbf{x}_s denotes the configuration of the neighbors in the solid at density ρ . For the calculation of fluid properties, ϕ must be averaged over many configurations of neighbors that are different from those of the solid. Since current theories of the electronic structure of matter are not sufficiently accurate for calculating ϕ , except for very simple systems, the CRIS model idealizes the fluid configurations and approximates ϕ by [10]

$$\phi \approx (\rho/\rho_s) E_c(\rho_s). \quad (9)$$

Here ρ is the actual density of the fluid, and ρ_s is the solid density having the same nearest neighbor distance as that of the given fluid configuration.

For materials like iron, with more than one solid phase, there is ambiguity as to which zero-Kelvin isotherm E_c to use in Eq. (9). However, our experience has shown that E_c for the most dense solid phase tends to give the best predictions of the fluid properties. In this work, therefore, we use the same function E_c for the fluid as for the hcp (ϵ) phase. As a result, the cohesive energy ΔE_b is also the same for both phases.

It is well-known that perturbation theory can be used to expand the free energy A_ϕ about the properties of a hard-sphere fluid [10],

$$A_\phi(\rho, T) = A_0(\rho, T, \sigma) + (N/W) \langle \phi \rangle_0 + \Delta A. \quad (10)$$

Here A_0 is the free energy for a fluid of hard spheres with diameter σ , and $\langle \phi \rangle_0$, the first-order correction, is an average of ϕ over all configurations of the hard sphere fluid. By definition, ΔA includes all corrections to the first two terms.

In the CRIS model, the hard-sphere diameter σ is defined by a variational principle that minimizes $|\Delta A|$. The correction terms are then computed from approximate expressions. The variational principle insures that the structure of the hard-sphere system used in the perturbation expansion is close to that of the real fluid. We have previously demonstrated that this approach does in fact give good results for the structure factor of iron, and also its shear viscosity [3] [10].

The following additional steps were taken to “fine tune” the fluid model to give the best possible agreement with experimental data for liquid iron. First, the Panda LJ MATCH option, which defines the behavior of the zero-Kelvin isotherm in tension [8], was used to adjust the liquid density at the melting point [22]. Second, the parameter EFAC, an empirical correction to Eq. (9) [8], was used to adjust the energy at the melting point [7]. Finally, we modified Panda so that the two integrals computed in the correction term ΔA could be multiplied by empirical factors, WX1 and WX2; these factors were used to adjust both the energy and the entropy at the melting point [7]. The values used were RLJ=7.5, FAC LJ=0.68, EFAC=0.23, WX1=WX2=2.1.

2.3 Thermal Electronic Contributions

At sufficiently high temperatures, excitation of electrons out of the ground state configuration can make an important contribution to the thermodynamic properties [23]. Most EOS models for iron have either ignored this term or attempted to represent it using simple free electron gas formulas. The model used here predicts that the thermal electronic term becomes important at temperatures above about 500K and that it makes a large contribution to the thermal expansion. The latter effect, which agrees with experimental data, is not predicted by the simpler models.

None of the existing theories for calculating thermal electronic contributions to the EOS give satisfactory results over the full density-temperature range of interest [23]. Therefore, we have synthesized this term by combining results from two theories - the INFERNO model of Liberman [24] for densities $\rho > 6 \text{ g/cm}^3$, and the Panda ionization equilibrium (IONEQ) model [8] for densities $\rho < 1 \text{ g/cm}^3$, with an average of the two models at intermediate densities. These data were combined to form a table of the electronic entropy, the features of which are depicted in Fig. 1. The other thermodynamic functions were computed by numerical differentiation and integration of the entropy, as described in Ref. [8]. The electronic pressure is shown in Fig. 2.

An important aspect of the electronic behavior of matter is the *insulator-metal transition* - the change of the valence electrons from localized, insulating states at low densities to delocalized, metallic states at high densities. Previous work showed that the INFERNO

model gives excellent predictions of the effect of this phenomenon on the shock Hugoniot of xenon, in which the transition is induced under pressure [3] [10]. In iron, the insulator-metal transition begins at a density of about 4 g/cm^3 , causing a pronounced drop-off in the entropy. At densities above about 20 g/cm^3 , the electrons behave like a simple free electron gas. The same phenomenon causes large thermal electronic contributions to the pressure in the density range $4 < \rho < 20$, as seen in Fig. 2.

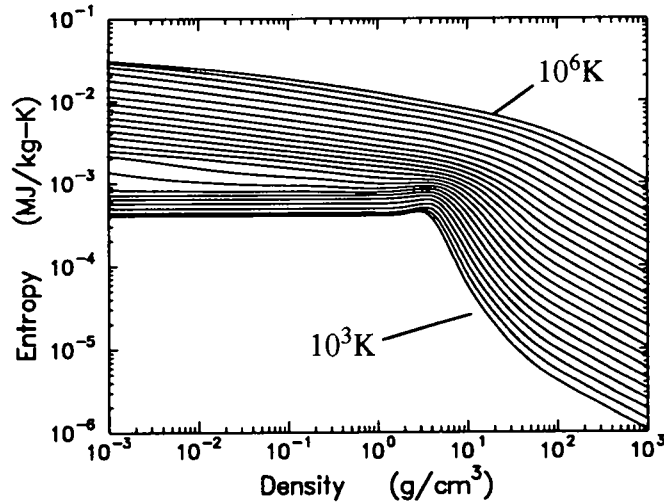


Fig. 1. Electronic contribution to the entropy for iron. Temperatures on the 25 isotherms shown range from 1.0×10^3 to $1.0 \times 10^6 \text{ K}$ and are equally spaced in the logarithm.

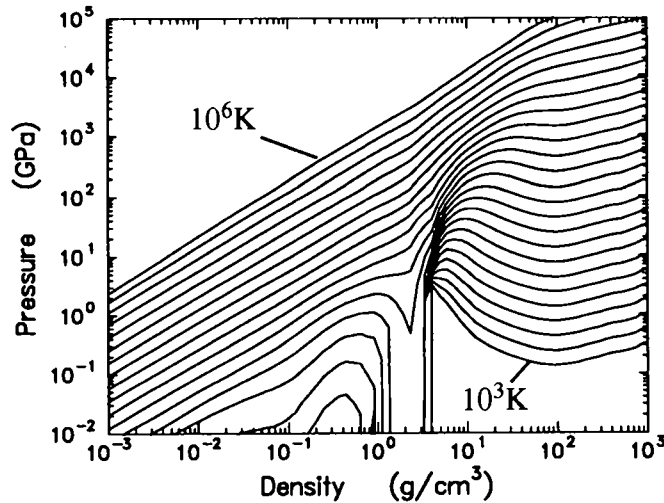


Fig. 2. Electronic contribution to the pressure for iron. Isotherms are the same as Fig. 1.

The INFERNO and IONEQ models both exhibit the basic features seen in Figs. 1 and 2. However, the INFERNO model is preferred in the high density regime because it has a more sophisticated and self-consistent treatment of the continuum lowering and metalliza-

tion effects. It predicts the low-temperature coefficient of the electronic specific heat to be 1.4×10^{-3} cal/mole/ K^2 , in excellent agreement with the value reported for the ϵ -phase [20], and only slightly higher than the value of 1.2×10^{-3} reported for the α -phase [7]. (The value for the α -phase may include magnetic effects that are ignored here.) The INFERNO calculations are also in good agreement with band theoretical calculations of Boness and Brown [25], which encompass densities and temperatures up to 14 g/cm^3 and $1.0 \times 10^4 \text{ K}$, respectively.

The switch to a different model at low densities is necessary because INFERNO uses an approximation for the statistics of the bound state configurations that is very inaccurate in the insulating regime. The calculations also become prohibitively expensive, due to the existence of many bound states. The IONEQ results are in fairly good agreement with those from INFERNO in the regime $\rho > 4$. However, some modifications to them were needed in order to make an entropy table that was smooth enough for computing the pressure by numerical differentiation. Additional details about construction of the electronic entropy table are given in Appendix A.

2.4 Multiphase EOS Calculations

After tabulating EOS for the α , γ , ϵ , and fluid phases, the Panda MOD TRN option [8] was used to compute the phase diagram and construct the multiphase EOS. The input for this option includes an energy shift for each phase, which was chosen to give zero energy for the α -phase at room temperature and solid density. In principle, the same energy shift should be used for all four phases, since all four tables have the same zero of energy. However, slightly different values were used in order to refine the predicted phase boundaries.

We were unable to find a satisfactory model for the α -phase that described both the low-temperature ($T < 1184 \text{ K}$) and high-temperature (δ -phase) regions. Therefore, a second table was made for the δ -phase. By adding a constant to the entropy ($WSL = 1.42$ [8]), and using a different energy shift than for the low-temperature region, it was possible to match the γ - δ transition temperature, melting temperature, and slope of the melting curve.

The energy shift for the ϵ -phase was chosen to make the α - ϵ phase boundary occur at 13.0 GPa , consistent with shock loading data, instead of the equilibrium value, 11.0 GPa .

The mesh used in making the multi-phase EOS table included 90 densities in the range $1.0 \times 10^{-6} \leq \rho \leq 1.0 \times 10^3$, plus a $\rho = 0$ point, and 70 temperatures in the range $0 \leq T \leq 1.2 \times 10^7$. The mesh points were chosen to give good resolution of the phase transitions and other important features of the EOS surface. In order to allow treatment of fracture models, a tension region was included at temperatures below the boiling point ($TSPALL = 3135$). In order to model the vaporization behavior, Maxwell constructions were performed at all higher temperatures, up to the critical point ($\approx 2.5 \times 10^4 \text{ K}$).

The new EOS table has been added to the SNL-SESAME library [11] (file "sesame") as material number 2150.

3. Results and Discussion

3.1 Thermophysical Data

Calculated curves of entropy and density, as functions of temperature, are shown in Figs. 3 and 4, respectively, along with experimental data [7] [21] [22]. To illustrate the importance of the thermal electronic contribution, we also show results obtained when this term is omitted. The electronic term makes a significant contribution to both the entropy and the density. It becomes important above about 500K and is quite large in the liquid phase.

The effect on density may explain anomalous behavior that is seen in the thermal expansion data of iron. Andrews pointed out that there is a hump in the thermal expansivity curve, in the range 400-900K, which cannot be fit using a standard treatment of the lattice vibrations and does not correlate with magnetic effects [1]. This behavior was tentatively ascribed to the presence of impurities [20]. However, the present work suggests that it is due to the large electronic pressure term shown in Fig. 2.

The general agreement with experimental data is quite good, although there is some deviation from the measured liquid entropy and density at high temperatures. (The entropy data at high temperatures are actually extrapolations that assume a constant heat capacity for the liquid [7].) Our theory of the thermal electronic contributions is admittedly weakest in the density range $1 < \rho < 6$, where the two models are being joined. Hence it is likely that most of the discrepancy arises from the treatment of that term.

Our calculated boiling point for iron is 3190K, quite close to the experimental value of 3135K [7]. The critical temperature, which is strongly influenced by the thermal electronic term, is predicted to be $\approx 2.5 \times 10^4$ K. There are no measurements of the critical point or the vaporization behavior at high temperatures.

3.2 Static Compression Data

In Fig. 5, we compare the room temperature isotherm computed using our model with the experimental data [14] - [18]. The insert in Fig. 5 shows data to a pressure of 300 GPa. The agreement is excellent up to 100 GPa, but our model is slightly softer than recent measurements relative to a Pt standard [18] at higher pressures. (We have used the extrapolation formula in this regime.) We have not been able to bring our curve into agreement with these data without spoiling our predictions of the shock data. Therefore, we have decided to accept this discrepancy, at least for the present.

As noted in Sec. 2.1, the model parameters were chosen to give good agreement with static measurements for α - and ϵ -phase iron at temperatures up to 723K [17], although we have not displayed those data here.

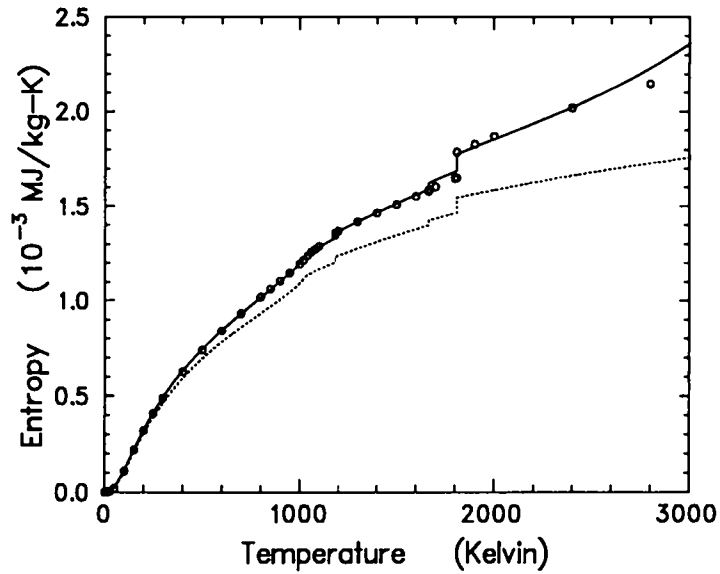


Fig. 3. Entropy vs. temperature for iron (zero pressure). The solid line is calculated including all terms, the dotted line omitting the thermal electronic term. Circles are experimental data [7].

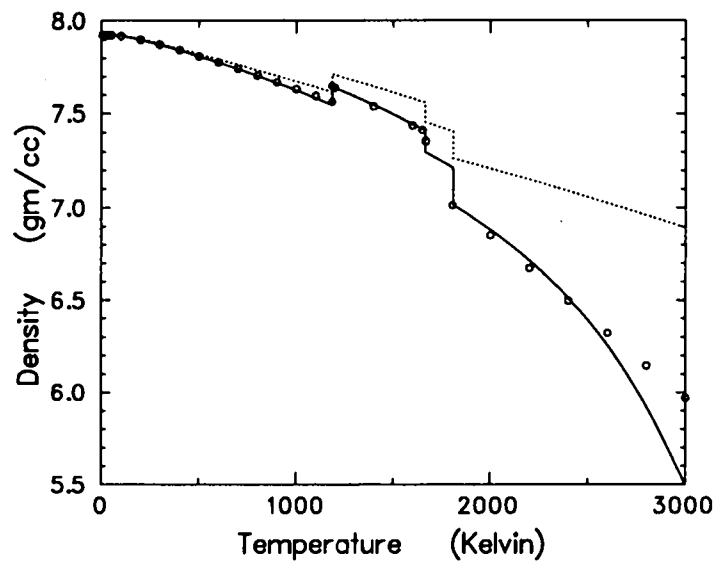


Fig. 4. Density vs. temperature for iron (zero pressure). The solid line is calculated including all terms, the dotted line omitting the thermal electronic term. Circles are experimental data [21] [22].

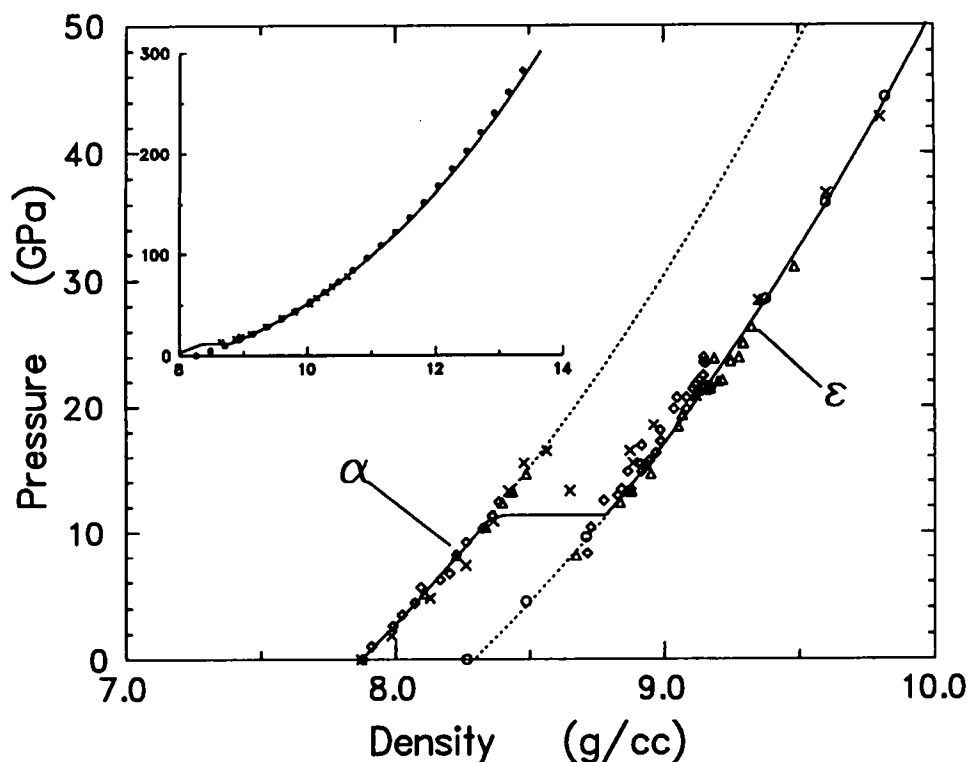


Fig. 5. Comparison of calculated room temperature isotherm (solid line) with diamond cell measurements: triangles - [14], x's - [16], diamonds - [17], circles - [18]. Dotted lines are extrapolations of the α and ϵ curves into their metastable regions. The insert shows data to higher pressures.

3.3 Phase Diagram

The calculated phase diagram is compared with experimental data [5] [26] [27] [28] [29] [30] in Fig. 6. (There is still considerable disagreement among various measurements of the α - ϵ phase boundary [5]; the points shown in Fig. 6 are merely representative.) Our results for the α - γ , α - ϵ , γ - ϵ , γ - δ , and δ -liquid phase boundaries are satisfactory.

The α - ϵ transition exhibits nonequilibrium and hysteretic behavior in both static [5] and dynamic [2] experiments. The transition typically occurs at about 13 GPa on loading and 9 GPa on unloading. That kind of behavior cannot be built into a single EOS table. In the present work, the energy of the ϵ -phase was shifted to match the 13 GPa transition when making the tabular EOS; the dotted curves in Fig. 6 show the phase boundaries corresponding to this case. This choice gives a good prediction of the multiple wave structure that is observed on shock loading, but does not accurately represent unloading behavior.

The CTH EOS package offers provisions for treating nonequilibrium and hysteretic effects using the "two-state" model [11] [12]. The α -phase could be omitted when making the EOS table and treated as the initial state, the progress of the transition being controlled by internal state variables. However, that approach has not been investigated in this work.

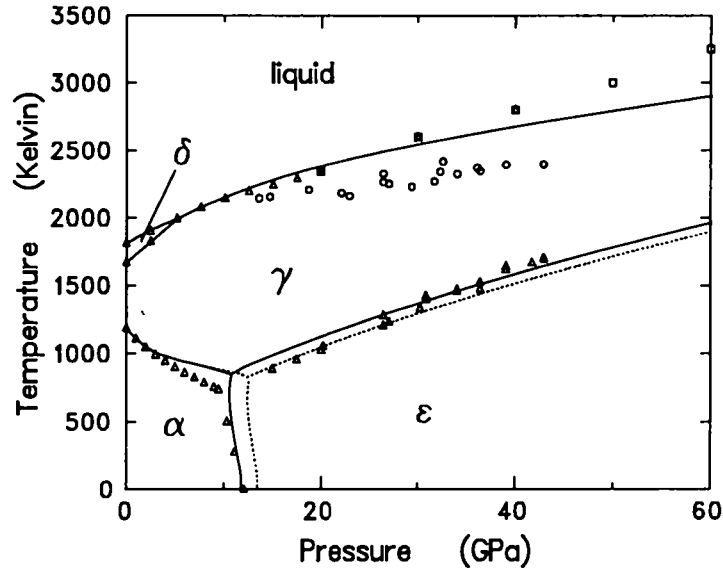


Fig. 6. Phase diagram for iron. Solid line shows equilibrium phase boundaries calculated using the model, and dotted lines show boundaries obtained when the ϵ -phase energy is shifted to give an α - ϵ transition pressure of 13.0 GPa. Experimental data are: triangles - [5] [26] [27] [28], circles - [29], squares - [30].

3.4 Melting

The melting curve and γ - ϵ phase boundary at high pressures are of considerable interest [4] but are not yet well known, experimentally. Our calculated melting curve agrees with the measurements of Strong, et al. [26] and Liu and Bassett [27] up to 20 GPa. At higher pressures, however, there is stark disagreement between the melting data of Boehler [29] and those of Williams, et al. [30]. Our calculated melting curve is intermediate between these two sets of data. However, additional insight into the behavior of these phase transitions at high pressures can be obtained from shock data [31], as discussed below.

3.5 Shock-Wave Behavior

Figure 7 shows the phase diagram and pressure-temperature Hugoniot loci for iron shocked from initial densities in the range 3.4 to 7.85 g/cm³. It can be seen that shock wave measurements for these initial densities sample the phase diagram over a wide range of temperatures and pressures. The calculated Hugoniots agree very well with experimental data [32] - [38] in the shock velocity-particle velocity plane, as shown in Fig. 8.

Brown and McQueen [31] have measured rarefaction wave velocities for iron, shock compressed to pressures between 77 and 400 GPa. They detected two discontinuities that they interpret as due to the ϵ - γ transition (200 ± 2 GPa,) and melting (243 ± 2 GPa). Our model correlates quite well with those results, shown by arrows in Fig. 7.

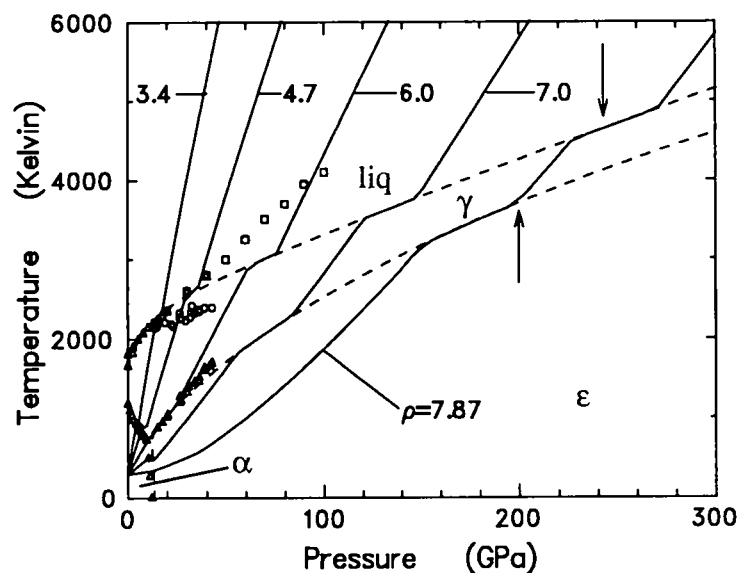


Fig. 7. Shock-induced phase transitions in iron. Solid lines are Hugoniot curves for various initial densities, as indicated, and dotted lines are calculated phase boundaries. Arrows show the pressures at which discontinuities in rarefaction wave velocity are observed in shock wave experiments [31]. Experimental data are the same as in Fig. 6.

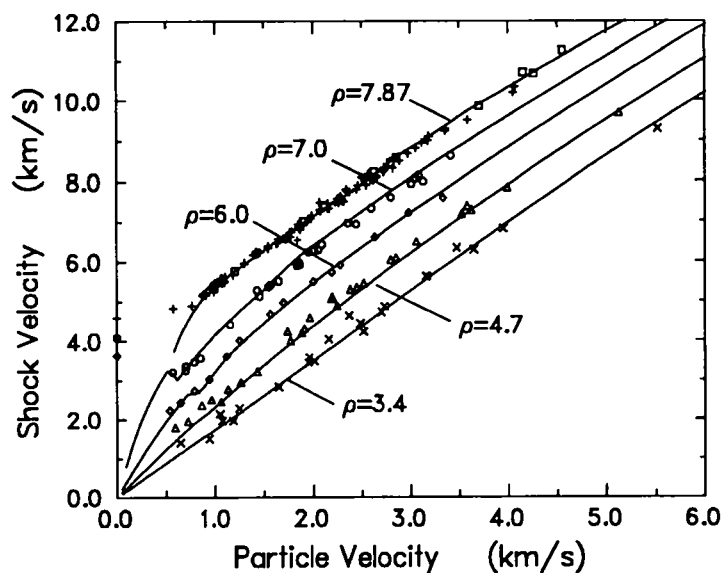


Fig. 8. Hugoniot for iron at various initial densities. Solid lines are calculated. Experimental data are from Refs. [32] - [38].

It should be noted that our model predicts a much lower temperature for shock melting than would be expected from the data of Williams, et. al. [30]. These authors observed that the point obtained by extending the ϵ -phase Hugoniot locus to 243 GPa agrees with an extrapolation of their data. However, that argument fails to account for the lower temperatures obtained after transition to the γ -phase. Our calculations also do not agree with the shock temperatures reported in this paper, but the accuracy of those measurements remains open to question [25]. Drastic changes in our model, which are not warranted by any other data, would be required to reconcile the melting curve of Ref. [30] with the sound speed measurements of Ref. [31]. Therefore, we believe that additional experimental studies of melting in iron are needed.

We further observe that our model predicts that the temperature on the ϵ - γ phase line reaches a maximum at a pressure of about 1×10^4 GPa and that there is no ϵ - γ -liquid triple point, in contrast to other theoretical treatments [4]. It may be possible to modify the parameters for the ϵ and γ phases to introduce a triple point near 300 GPa, without destroying the agreement with the shock melting pressure. However, we have not attempted to do so, since the existing experimental data do not require it.

3.6 RHA Steel

RHA (Rolled Homogeneous Armor) is a mild Ni-Cr steel that has a density and shock wave properties close to those of pure iron. RHA Hugoniot data, for both the α -phase [39] and ϵ -phase [40], are shown in Fig. 9, together with the data for iron [32] [41]. The solid lines show our calculations for an (ideal) initial density of 7.872 g/cm^3 and including the effects of material strength. (The elastic-perfectly plastic model was used with a yield strength and shear modulus of 0.7 GPa and 88.0 GPa, respectively.) The calculations for the α -phase show the elastic precursor with a velocity of 6.0 km/s and the plastic wave for $u_p < 0.32 \text{ km/s}$. For $0.32 < u_p < 0.89$, the calculations account for preshocking of the ϵ -phase by the plastic wave due to the phase transition. (The stress of the first plastic wave was found to be 13.4 GPa when strength was included.) The region $u_p > 0.89$ corresponds to a single plastic wave in the ϵ -phase. (Also see Sec. 4.1.)

Figure 9 shows that the α -phase Hugoniots for RHA [39] and iron [40] are virtually identical within experimental error. Both sets of data lie slightly below our calculations. However, this small discrepancy is eliminated if porosity is taken into account. The dotted line in Fig. 9 shows a calculation for an initial density of 7.84 g/cm^3 , which is typical of actual material samples. The ϵ -phase data for iron and RHA are also in close agreement.

Allowing for experimental uncertainties, there do not appear to be any significant differences between the EOS of iron and that of RHA (although their yield strengths differ). Therefore, we have not constructed a separate EOS table for RHA.

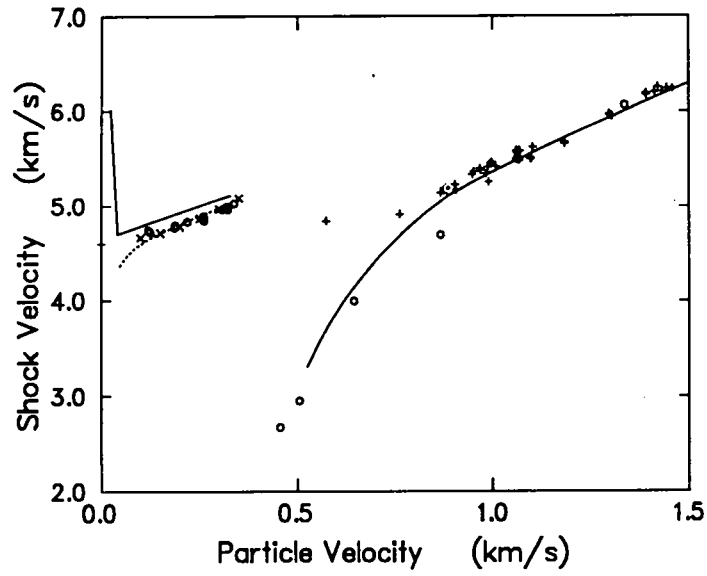


Fig. 9. Hugoniot data for iron and RHA steel. Solid lines are calculated for an initial density of 7.872 g/cm^3 , the dotted line for 7.84 g/cm^3 . Experimental data are: crosses - iron [32], x's - α -phase iron [41], circles - RHA [39] [40].

4. Hydrocode Calculations

4.1 Wave-Profile Measurements

Barker and Hollenbach [42] studied the impacts of iron plates on iron targets at velocities ranging from 0.61 to 1.9 km/s (loading stresses from 12 to 40 GPa). Figure 10 compares CTH calculations, made with our new tabular EOS, with the measured free surface velocities for six of these experiments. The nominal thickness of both the impactor and the target was 0.64 cm in each of these tests. The CTH calculations used a zone size of 0.0032 cm, the elastic-perfectly plastic model with a yield strength and Poisson's ratio of 0.7 GPa and 0.285, respectively, and a fracture strength of 3.8 GPa.

The calculations are in good agreement with the experimental VISAR data. The first wave in all cases is the elastic precursor. Tests 1, 2, 18, and 17 show two plastic waves, the first one being due to the 13 GPa phase transition, and the second being subsequent loading of the ϵ -phase. The phase transition is just at the point of being overdriven in test 6, and is completely overdriven in test 10. Note that the elastic precursor is determined by the properties of the α -phase, even in test 10.

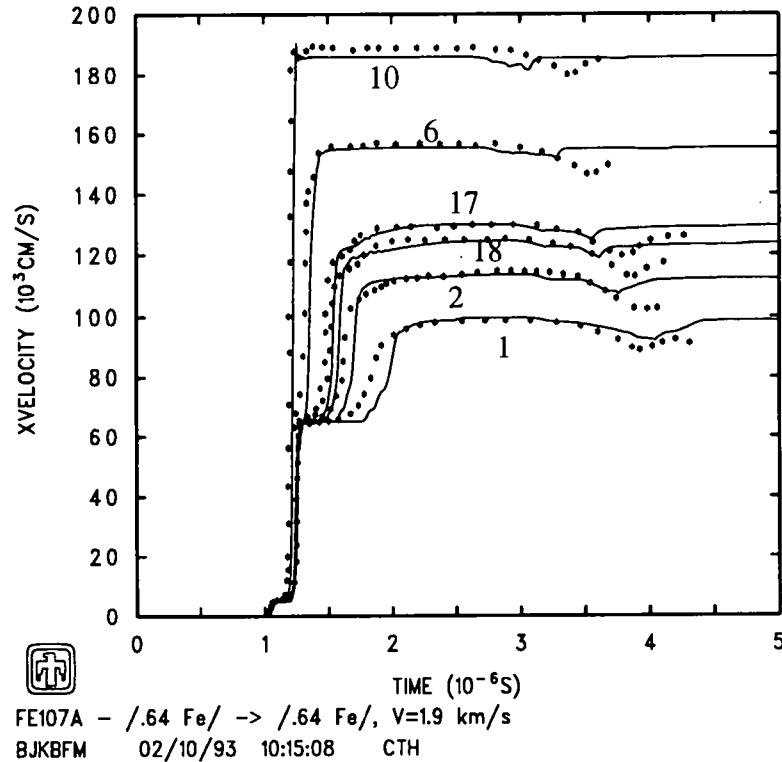


Fig. 10. Calculated free surface velocities for symmetric impacts of 0.64 cm iron plates. Test numbers are given in Ref. [42] and correspond to the following impact velocities: 1 - 0.99, 2 - 1.15, 18 - 1.25, 17 - 1.31, 6 - 1.57, 10 - 1.87 km/s. Discrete points are the experimental data.

Barker and Hollenbach also investigated the unloading behavior of iron in two experiments with a sapphire impactor and a sapphire window, at velocities below the 13 GPa phase transition. Our CTH calculations for their test 15, having an impact velocity of 0.4825 km/s and peak stress of 10.26 GPa, are compared with the measurements (shown by points) in Fig. 11. As noted in the original paper, a calculation using the elastic-perfectly plastic model (shown by the solid line) does not match the unloading behavior. The initial elastic release arrives too early and is too large. For reference, a purely hydrodynamic calculation is also shown (dashed line). The fact that the observed behavior falls in between these two calculations shows that the shocked state retains some strength, but that it is significantly reduced [42].

None of the constitutive models currently used in CTH and other “production” hydrocodes account for this anomalous behavior in iron. The resulting errors in predictions of unloading behavior could have some effect on the comparisons with more complicated experiments, such as those discussed below.

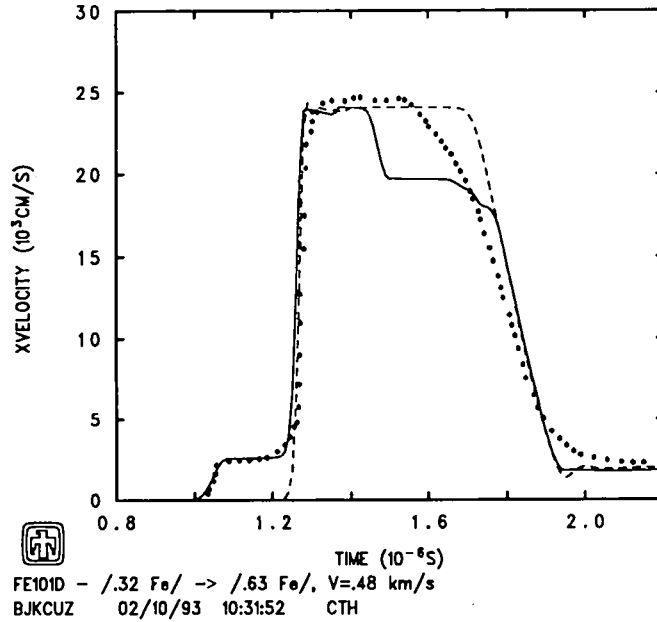


Fig. 11. Calculated velocity at sapphire window for test number 15 of Ref. [42]. The solid line was computed using the elastic-perfectly plastic model, the dashed line using a purely hydrodynamic model. Discrete points are the experimental data.

4.2 Nylon Ball Impact on Iron

Bertholf, et. al. [43] have analyzed an experiment in which a 0.953 cm nylon ball was used to impact a 1.27 cm steel plate with a velocity of 5.182 km/s. Their numerical simulations showed that it was necessary to include the α - ϵ phase transition in the EOS in order to reproduce the observed back-surface spallation of the steel plate.

Our calculations of this experiment, using the CTH code and our new tabular EOS, are shown in Fig. 12. The predictions depend not only on the EOS but are also very sensitive to the treatment of material strength and fracture. In this calculation, we used the Johnson-Cook plasticity model, with parameters for RHA steel [44], and the Johnson-Cook fracture model for steel, with the fracture strength set to 3.8 GPa [43]. The nylon EOS was treated the same as in Ref. [43]. The zone size was 0.032 cm.

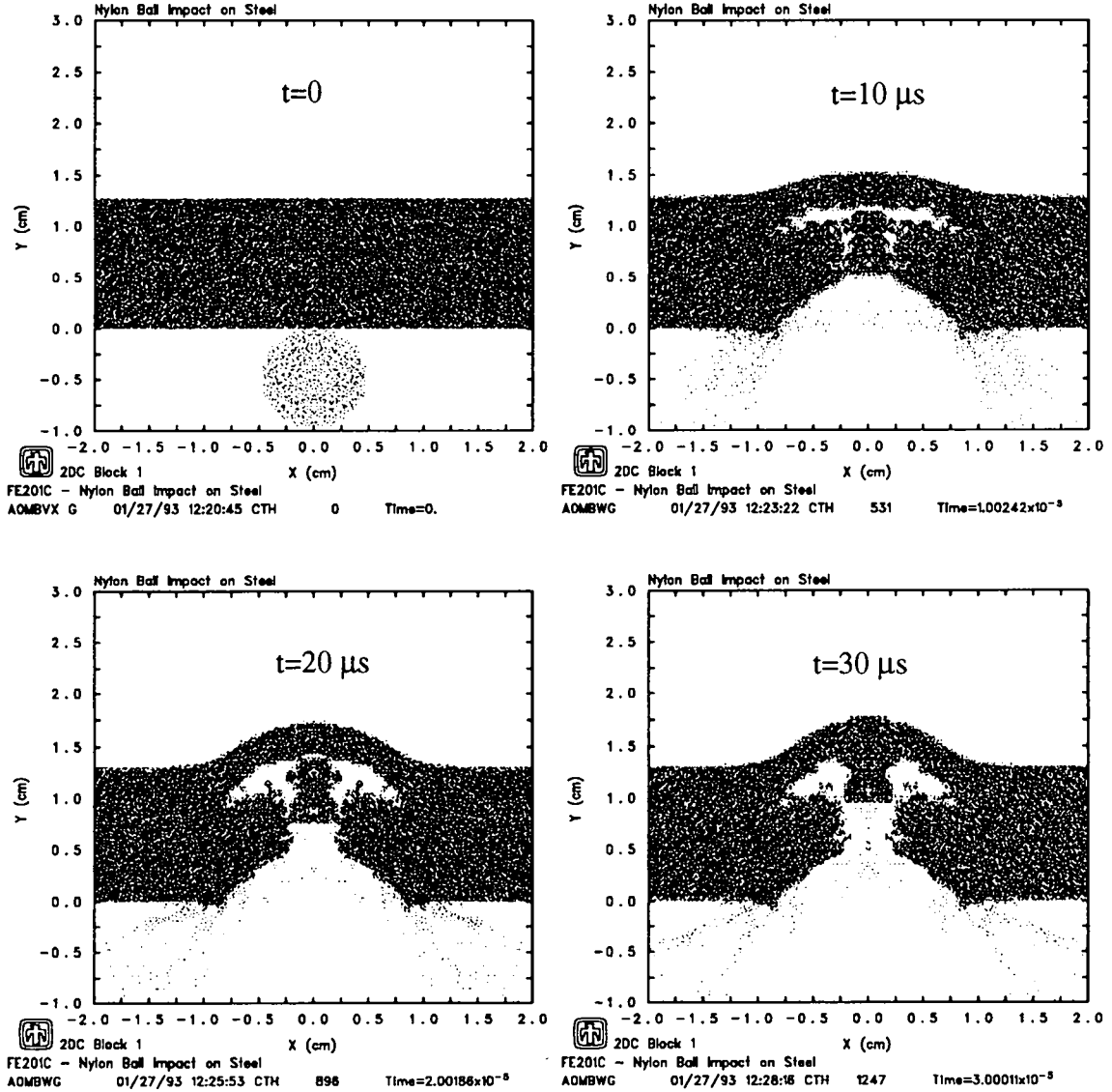


Fig. 12. CTH calculations of nylon ball impacting steel plate.

The principal features of the event, as seen in Fig. 12, are as follows. By 10 μs , the nylon ball has been vaporized and has formed a crater with a depth nearly half the target thickness. Reflection of the impulse from the back surface of the plate has resulted in spallation, opening up a gap. A cylindrical fracture surface has also formed, resulting in a plug of target material. The frames at 20 and 30 μs show the motion of this plug toward the

back surface, opening the gap still further. The existence of the plug and the opening of a wide gap both agree with the experimental data [43].

The dependence of the results on the material parameters is illustrated in Fig. 13. Figure 13a shows a calculation (at 30 μ s) identical to that of Fig. 12, except that the iron EOS table was replaced by a Mie-Grüneisen EOS with no phase transition [45]. There is no evidence of a cylindrical plug, showing that the α - ϵ phase transition is needed to predict that phenomenon. The calculation shown in Fig. 13b (also at 30 μ s) is identical to that of Fig. 12, except that the plasticity parameters for 4340 steel were used instead of those for RHA [44]. Since the strength of 4340 steel is 15% higher than that of RHA, the spall cavity is smaller; the cylindrical plug has formed but has not yet broken loose.

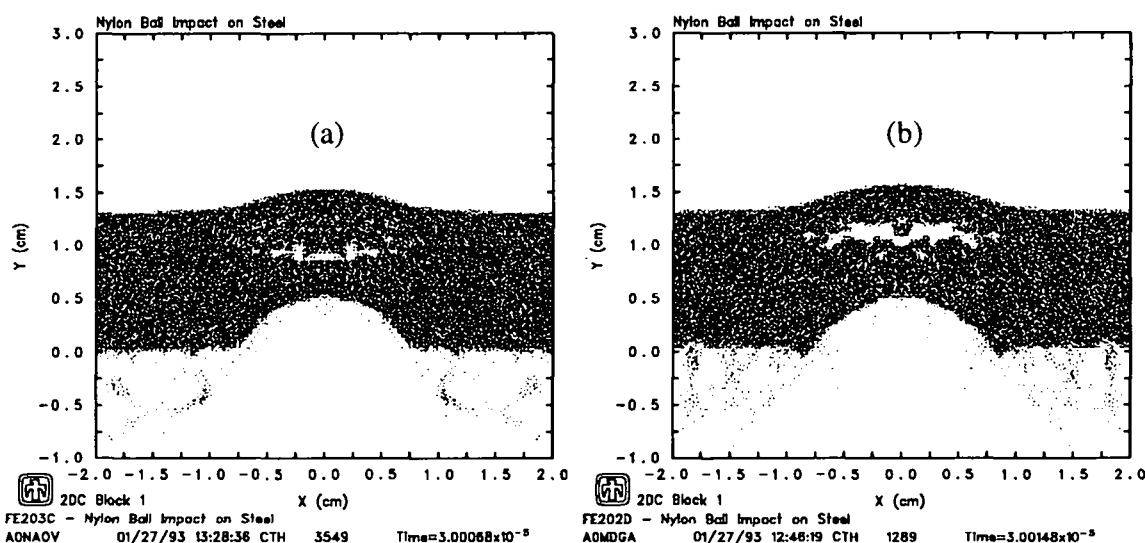


Fig. 13. Sensitivity of nylon-steel impact problem to EOS and material strength: (a) - calculation with Mie-Grüneisen EOS [45], (b) - calculation with 4340 parameters [44]. Both calculations are at 30 μ s.

4.3 Shaped Charge Perforation of RHA Steel

Raftenberg [45] has studied the perforation of a 1.3 cm RHA plate by a shaped charge jet of OFHC copper. He found that the perforation was accomplished by the leading jet particle alone; the velocity (7.73 km/s) and geometry of this particle were determined from radiographs. The splash and debris patterns of the target were recorded on a radiograph taken 36 μ s after impact. The recovered target was sectioned to determine the size and shape of the hole created by the event.

Raftenberg simulated his experiment using a Lagrangian code with an eroding slide line and a simple Mie-Grüneisen EOS with no phase transition. He predicted much too small a

hole using only a tensile failure model, but he was able to obtain reasonable results with a model that included shear band failure effects [45].

Figure 14 shows CTH calculations of this experiment, using our new tabular EOS, the elastic-perfectly plastic model with a yield strength of 1.5 GPa and including thermal softening, and the Johnson-Cook fracture model with a fracture strength of 3.8 GPa. The zone size was 0.0325 cm. The calculations are in very good agreement with the size and shape of the hole observed in the recovered plate (shown by the dark band at 100 μ s). The calculated material distribution at 36 μ s is also consistent with the radiograph (see Ref. [45]).

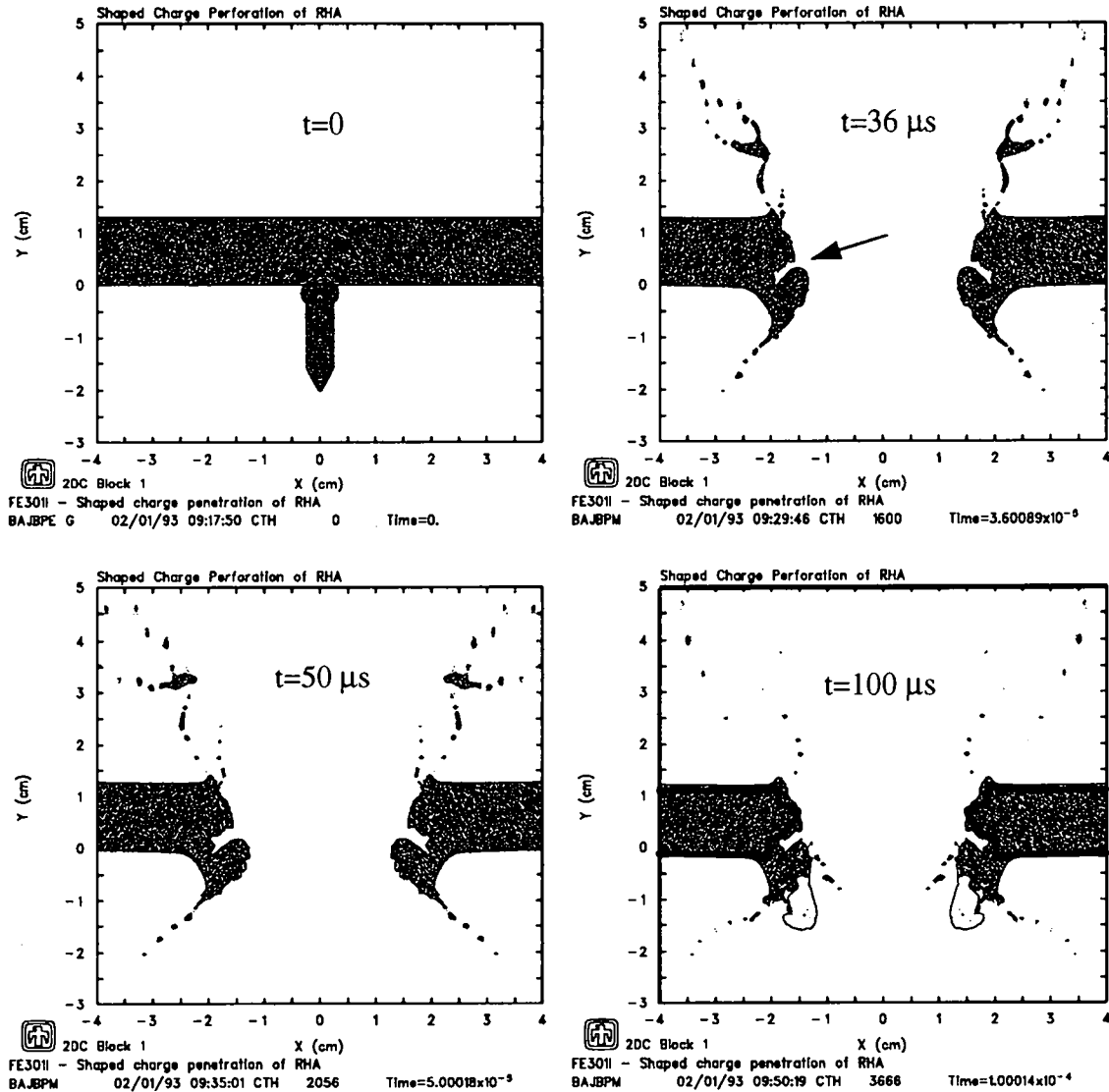


Fig. 14. CTH calculations of perforation of RHA plate by shaped charge jet. The measured hole contours are shown by the dark band on the 100 μ s frame.

An interesting feature of the calculation is the opening of a crack, indicated by an arrow on the 36 μ s frame of Fig. 14, and splitting off of a large piece of material at the hole entrance. (This piece should eventually separate completely from the plate, although the CTH calculations have not predicted it to occur by 100 μ s.) These features are consistent with observations of the recovered plate, including the fact that the entrance hole was larger than the exit hole.

To illustrate the effect of the EOS on the numerical predictions, Fig. 15 shows the results (at 36 μ s) obtained using two other EOS models, but with the same strength and fracture parameters as in Fig. 14. Raftenberg's Mie-Grüneisen EOS [45] with no phase transition was used in Fig. 15a, while the ANEOS model discussed by Bertholf, et. al. [43] was used in Fig. 15b. (The ANEOS model includes the α - ϵ phase transition but ignores melting and other features built into our new EOS; a tabular version, material number 2141 [12], was used in this calculation.) Both calculations show about the same size hole as obtained with our new EOS, but the debris pattern and the behavior near the entrance hole are quite different from those seen in Fig. 14.

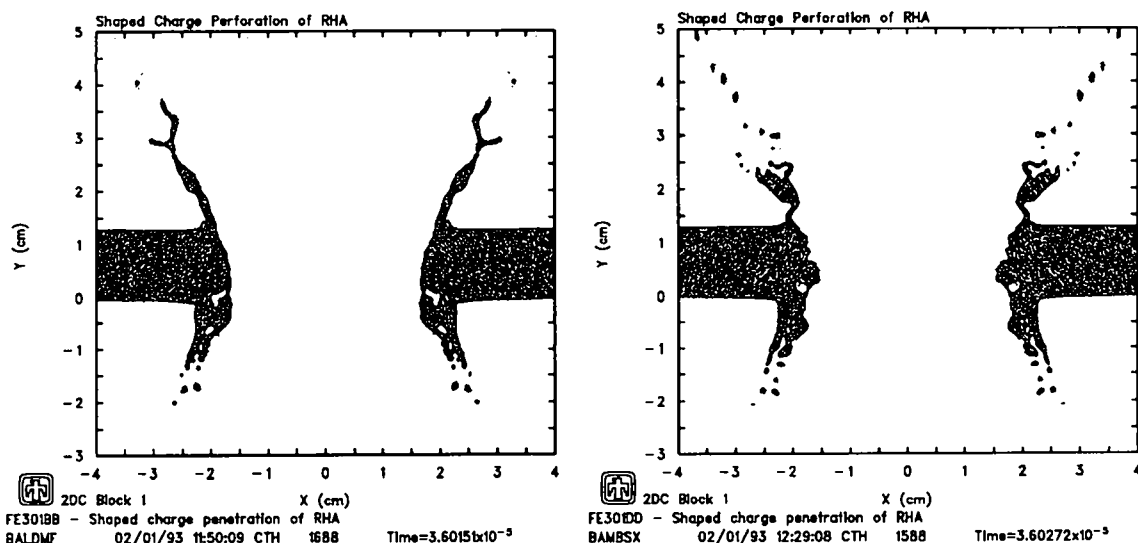


Fig. 15. Sensitivity of RHA perforation problem to EOS: (a) calculation with Mie-Grüneisen EOS [45], (b) - calculation with ANEOS model [12] [43].

However, we must emphasize that the fracture and elastic-plastic models also have a tremendous effect on the predicted results. When the default CTH fracture model is used, the crack discussed above does not appear, although the material distribution at 36 μ s is close to that seen in Fig. 14, otherwise. Surprisingly, the Johnson-Cook plasticity model also gives poor results for this problem. We do not know the reason for this fact, although the levels of stress, strain, temperature, and strain rate encountered in this problem are far outside the regime for which the model was calibrated [44]. Finally, we note that our two-dimensional CTH calculation does not allow fragmentation of the material splitting off from the plate at the entrance hole, an inherently three-dimensional effect.

5. Conclusions

We have developed a new tabular equation of state (EOS) for iron, which includes treatment of solid-solid phase transitions, melting, vaporization, and thermal electronic excitation. The EOS is in good agreement with experimental thermophysical data, static compression data, phase boundaries, and shock-wave measurements. Hydrocode calculations of plate impact tests, the impact of a nylon ball on a steel plate, and the perforation of an RHA steel plate by a shaped charge are also in good agreement with experiment.

In connection with future work, the following points should be considered.

- The model predicts a lower melting temperature at high pressures than has been found in previous analyses. Additional experimental work is required to resolve the differences between existing data and to test the present predictions.
- This EOS does not account for the nonequilibrium and hysteretic behavior of the α - ϵ phase transition. Future extensions of this work could include use of a “two-state” model, with internal state variables, to treat such effects.
- The study of complicated impact experiments shows that the EOS can have a significant effect on hydrocode predictions. However, these predictions are also very dependent on the plasticity and fracture models that are used.
- The study of plate impact experiments shows that existing plasticity models for iron are not satisfactory. In particular, they do not account for the loss of strength in the vicinity of the α - ϵ phase transition and its effect on shock unloading behavior.

Finally, we note that the EOS discussed in this report is applicable only to pure iron and to mildly alloyed steels, such as RHA. It should not be used for stainless steels and other alloys which have significantly different phase boundaries. We have not attempted to construct EOS for such materials, although the present work does lay the foundation for doing that in the future.

References

- [1] D. J. Andrews, "Equation of State of the Alpha and Epsilon Phases of Iron," J. Phys. Chem. Solids **34**, 825 (1973), and references therein.
- [2] G. E. Duvall and R. A. Graham, "Phase Transitions Under Shock Wave Loading," Rev. Mod. Phys. **49**, 523-579 (1977), and references therein.
- [3] G. I. Kerley, "Theoretical Model of Liquid Metals," in Proceedings of the Eighth Symposium on Thermophysical Properties, J. V. Sengers (Ed.) (Am. Soc. Mech. Engineers, New York, NY, 1982) Vol II, pp. 159-164.
- [4] O. L. Anderson, "Properties of Iron at the Earth's Core Conditions," Geophys. J. R. astr. Soc. **84**, 561-579 (1986), and references therein.
- [5] J. M. Besson and M. Nicol, "An Equation of State of γ -Fe and Some Insights About Magnetoelastic Effects on Measurements of the α - γ - ϵ Triple Point and Other Transitions," J. Geophys. Res. **95**, 21,717-21,720 (1990), and references therein.
- [6] J. F. Cannon, "Behavior of the Elements at High Pressures," J. Phys. Chem. Ref. Data **3**, 781-824 (1974).
- [7] R. Hultgren, P. D. Desai, D. T. Hawkins, M. Gleiser, K. K. Kelley, and D. D. Wagman, *Selected Values of the Thermodynamic Properties of the Elements* (American Society for Metals, Metals Park, Ohio, 1972).
- [8] G. I. Kerley, "User's Manual for PANDA II: A Computer Code for Calculating Equations of State," Sandia National Laboratories report SAND88-2291, 1991.
- [9] G. I. Kerley, "Equations of State for Calcite Minerals. I. Theoretical Model for Dry Calcium Carbonate," High Pressure Research **2**, 29-47 (1989).
- [10] G. I. Kerley, "A Model for the Calculation of Thermodynamic Properties of a Fluid Using Hard-Sphere Perturbation Theory and the Zero-Kelvin Isotherm of the Solid," in Molecular Based Study of Fluids, edited by J. M. Haile and G. A. Mansoori (Am. Chem. Soc., Washington, DC., 1983) pp 107-138.
- [11] G. I. Kerley, "CTH Reference Manual: The Equation of State Package," Sandia National Laboratories report SAND91-0344, 1991.
- [12] G. I. Kerley, "CTH Reference Manual: Porosity and Reactive Burn Models," Sandia National Laboratories report SAND92-0553, 1992.
- [13] L. Brewer, "The Cohesive Energies of the Elements," Lawrence Berkeley Laboratory report LBL-3720 (1975).

- [14] H.-K. Mao, W. A. Bassett, and T. Takahashi, "Effect of Pressure on Crystal Structure and Lattice Parameters of Iron up to 300 kbar," *J. Appl. Phys.* **38**, 272-276 (1967).
- [15] H. K. Mao and P. M. Bell, "Equations of State of MgO and ϵ Fe Under Static Pressure Conditions," *J. Geophys. Res.* **84**, 4533-4536 (1979).
- [16] A. P. Jephcoat, H. K. Mao and P. M. Bell, "Static Compression of Iron to 78 GPa With Rare Gas Solids as Pressure-Transmitting Media," *J. Geophys. Res.* **91**, 4477-4684 (1986).
- [17] E. Huang, W. A. Bassett, and P. Tao, "Pressure-Temperature-Volume Relationship for Hexagonal Close Packed Iron Determined by Synchrotron Radiation," *J. Geophys. Res.* **92**, 8129-8135 (1987).
- [18] H. K. Mao, Y. Wu, L. C. Chen, J. F. Shu, and R. J. Hemley, "Pressure Calibration to 304 GPa on the Basis of X-ray Diffraction Measurements of Pt, Fe, and CsI," *High Press. Res.* **5**, 773-775 (1990).
- [19] B. K. Godwal, S. K. Sikka, and R. Chidambaram, "Equation of State Theories of Condensed Matter Up To About 10 TPa," *Phys. Rep.* **102**, 121-197 (1983).
- [20] G. L. Stepanoff and L. Kaufman, "Thermodynamic Properties of h.c.p. Iron and Iron-Ruthenium Alloys," *Acta Metall.* **16**, 13-22 (1968).
- [21] Y. S. Touloukian, R. K. Kirby, R. E. Taylor, and P. D. Desai, *Thermophysical Properties of Matter (IFI/Plenum, New York) Vol. 12*, pg. 2.
- [22] A. V. Grosse and A. D. Kershenbaum, "The Densities of Liquid Iron and Nickel and An Estimate of Their Critical Temperature," *J. Inorg. Nucl. Chem.* **25**, 331-334 (1963).
- [23] A concise discussion of the theoretical problems associated with calculating the effects of thermal electronic excitation can be found in: J. R. Asay and G. I. Kerley, "The Response of Materials to Dynamic Loading," *Int. J. Impact Engng.* **5**, 69-99 (1987).
- [24] D. A. Liberman, "Self-Consistent Field Model for Condensed Matter," *Phys. Rev. B* **20**, 4981-4989 (1979).
- [25] D. A. Boness and J. M. Brown, "The Electronic Band Structures of Iron, Sulfur, and Oxygen at High Pressures and the Earth's Core," *J. Geophys. Res.* **95**, 21721-21730 (1990). The heat capacity curves from INFERNO are about 30% lower than those shown in Fig. 7 of this paper but are in good agreement if the density is shifted by the amount needed to correct the error in the authors' calculated zero-Kelvin curve, shown in their Fig. 1.
- [26] H. M. Strong, R. E. Tuft, and E. E. Hanneman, "The Iron Fusion Curve and γ - δ -l Triple Point," *Metall. Trans.* **4**, 2657 (1973).

- [27] L.-G. Liu and W. A. Bassett, "The Melting of Iron up to 200 kbar," *J. Geophys. Res.* **80**, 3777-3782 (1975).
- [28] E. Huang, W. A. Bassett, and P. Tao, "Study of bcc-hcp Iron Phase Transition by Synchrotron Radiation," in *High-Pressure Research in Mineral Physics*, edited by M. H. Manghnani and Y. Syono (AGU, Washington, D.C., 1987) pp. 165-172.
- [29] R. Boehler, "The Phase Diagram of Iron to 430 kbar," *Geophys. Res. Lett.* **13**, 1153-1156 (1986).
- [30] Q. Williams, R. Jeanloz, J. Bass, B. Svendsen, and T. J. Ahrens, "The Melting Curve of Iron to 250 Gigapascals: A Constraint of the Temperature of the Earth's Core," *Science* **236**, 181-182 (1987).
- [31] J. M. Brown and R. G. McQueen, "Phase Transitions, Grüneisen Parameter, and Elasticity for Shocked Iron Between 77 GPa and 400 GPa," *J. Geophys. Res.* **91**, 7485-7494 (1986), and earlier references cited therein.
- [32] S. P. Marsh, *LASL Shock Hugoniot Data* (University of California, Berkeley, 1980).
- [33] L. V. Altshuler, K. K. Krupnikov, B. N. Ledenev, V. I. Zhuchikhin, and M. I. Brazhnik, *Sov. Phys-JETP* **7**, 606 (1958).
- [34] L. V. Altshuler, S. B. Kormer, M. I. Brazhnik, L. A. Vladmirov, and A. I. Funtikov, *Sov. Phys-JETP* **11**, 766 (1960).
- [35] L. V. Altshuler, S. B. Kormer, A. A. Bakanova, and R. F. Trunin, *Sov. Phys-JETP* **11**, 573 (1960); *Sov. Phys-JETP* **15**, 65 (1962).
- [36] K. K. Krupnikov, A. A. Bakanova, M. I. Brazhnik, and R. F. Trunin, *Sov. Phys-JETP* **8**, 205 (1963).
- [37] L. V. Al'tshuler, A. A. Bakanova, L. P. Dudoladov, E. A. Dynin, R. F. Trunin, and B. S. Chekin, "Shock Adiabatic Curves of Metals. New Data, Statistical Analysis, and General Laws," *Sov. J. Appl. Mech. Tech. Phys.* **22**, 145-169 (1981)
- [38] R. F. Trunin, A. B. Medvedev, A. I. Funtikov, M. A. Podurets, G. V. Simakov, and A. G. Sevast'yanov, "Shock Compression of Porous Iron, Copper, and Tungsten, and Their Equation of State in the Terapascal Pressure Range," *Sov. Phys. JETP* **68**, 356-361 (1989).
- [39] G. E. Hauver, "The Alpha-Phase Hugoniot of Rolled Homogeneous Armor," USA Ballistic Research Laboratories report BRL-MR-2651, (1976).
- [40] G. Hauver and A. Melani, "The Epsilon-Phase Hugoniot of Rolled Homogeneous Armor," USA Ballistic Research Laboratories report ARBRL-MR-02909, (1979).

- [41] W. Arnold and W. Sachs, "Measuring and Simulation of Steady Shock Wave Profiles in Armco Iron," in *Shock Waves in Condensed Matter - 1989*, edited by S. C. Schmidt, J. N. Johnson, and L. W. Davison(North-Holland, Amsterdam, 1990) pp. 337-340.
- [42] L. Barker and R. E. Hollenbach, "Shock Wave Study of the $\alpha \leftrightarrow \epsilon$ Phase Transition in Iron," *J. Appl. Phys.* **45**, 4872-4887(1974).
- [43] L. D. Bertholf, L. D. Buxton, B. J. Thorne, R. K. Byers, A. L. Stevens, and S. L. Thompson, "Damage in Steel Plates From Hypervelocity Impact. II. Numerical Results and Spall Measurement," *J. Appl. Phys.* **46**, 3776-3783 (1975).
- [44] G. T. Gray III, S. R. Chen, W. Wright, and M. F. Lopez, "Constitutive Equations for Annealed Metals Under Compression at High Strain Rates and High Temperatures," Los Alamos National Laboratory, Oct. 1992.
- [45] M. N. Raftenberg, "Modeling RHA Plate Perforation by a Shaped Charge Jet," Ballistic Research Laboratory report BRL-TR-3363, June 1992.
- [46] G. I. Kerley, "Atomic Orbital Data for Elements with Atomic Numbers $1 \leq Z \leq 103$," Sandia National Laboratories report SAND88-2594, 1988.
- [47] R. D. Cowan, *The Theory of Atomic Structure and Spectra* (University of California, Berkeley, 1981) pp. 12-15.

Appendix A

Calculation of Thermal Electronic Entropy Table

The INFERNO calculations reported here were carried out using version 41 of the code, obtained from D. A. Liberman. The entropy was computed at 24 densities, exponentially spaced on the interval $0.6 \leq \rho \leq 600$, and at 28 temperatures, exponentially spaced on the interval $2.3 \times 10^3 \leq T \leq 1.2 \times 10^7$. These results were previously discussed in Refs. [3] and [10].

The Panda IONEQ model [8] computes ionization potentials, energy levels, and statistical weights for atomic ions from a scaling model, using a table of orbital radii and energies for the ground state configuration of the isolated atom [46]. In the present work, the binding energies EA for occupied orbitals were modified to improve agreement between the model predictions and experimental ionization potentials [47]. The old values [46] and modified values (in Hartree) are as follows:

Orbital	EA (old)	EA (mod)
1S+	-2.6394e+02	-2.6394e+02
2S+	-3.2536e+01	-3.0000e+01
2P-	-2.7966e+01	-2.7000e+01
2P+	-2.7441e+01	-2.7000e+01
3S+	-4.3237e+00	-4.1000e+00
3P-	-2.9734e+00	-2.9000e+00
3P+	-2.7538e+00	-2.7000e+00
3D-	-6.3675e-01	-5.0000e-01
3D+	-6.0859e-01	-4.7000e-01
4S+	-2.7116e-01	-2.9765e-01

The IONEQ results were generated using parameter settings $\text{MX}=\text{EFAC}=3$, $\text{F1}=\text{F2}=1$, $\text{KS}=5$. (The parameter MX is related to the number of allowed configurations, and the parameter KS is used to smooth the entropy table. See the Panda manual [8] for an explanation of the parameters.) The entropy was computed at 50 densities, exponentially spaced on the interval $1.0 \times 10^{-6} \leq \rho \leq 1.0 \times 10^3$, and at 50 temperatures, exponentially spaced on the interval $1.0 \times 10^2 \leq T \leq 1.2 \times 10^8$.

The IONEQ results are quite similar to those from INFERNO; they even agree with the behavior of the entropy isotherms in the insulator-metal transition region. However, the IONEQ model predicts somewhat lower entropies than INFERNO at temperatures in the vicinity of $5.0 \times 10^5 \text{K}$. We cannot explain the reason for this discrepancy. In any case, the mismatch leads to spurious structure in the pressure when the two data sets were merged to make a composite table. In order to eliminate this problem, the IONEQ entropies were

shifted by subtracting the difference between the IONEQ and INFERNO results at $\rho = 4$ and $1.0 \times 10^5 < T < 1.0 \times 10^6$ at all densities. The transition region was further smoothed by averaging the IONEQ and INFERNO results in the range $1 < \rho < 6$.

Appendix B

Output File for Multiphase EOS Calculation

THE PANDA CODE, UCS VERSION 2.05, 09/09/92
SANDIA NATIONAL LABORATORIES, ALBUQUERQUE, NM 87185

PROBLEM: IRON_EOS DATE: 01/26/93

OPTION?

@doit

!*****

!

! File dated 01/19/93 - Equation of state for alpha-phase iron.
! Tabular cold curve is Birch-Murnaghan fit to static data, with
! R0=7.969, B0=173.0, B0P=4.80. Thermal electronic term is included.
! A tabular term describes the magnetic contribution, which is
! computed from an magnetic specific heat given by:
! for T<= 1042K, CVE = T**1.5/(1080-T)/55.0 cal/mole/K
! for T > 1042K, CVE = 0.
! The energy zero is set to zero density and temperature.

!

!*****

! Setup

sym eb=7.469 seb=-7.469 ro=7.969 bo=173 gam=1.70 deb=425

OPTION?

!

mod sol crv=1 nuc=1 tel=1 tab=1 esft=seb

SOLID-LIQUID MODEL - ENTER MOLECULAR FORMULA

fe

MOLES = 1.0000E+00, Z = 2.6000E+01, AW = 5.5847E+01

FZ = 2.6000E+01, FW = 5.5847E+01, ZAV = 2.6000E+01

ENTER ECOH, RHOREF, TREF, GAMREF, DEBREF, CB, PSSN

7.397 7.873 298 gam deb

COLD CURVE - ENTER ICLD, RTFD, RLJ, FACLJ

4 11 7.0 1

ENTER NAME OF INPUT FILE

tty

ENTER DENSITY AND PRESSURE, POINT BY POINT

6.5000E+00 -2.1681E+01

6.7500E+00 -1.9321E+01

7.0000E+00 -1.6452E+01

7.2500E+00 -1.3046E+01

7.5000E+00 -9.0743E+00

7.7500E+00 -4.5092E+00

8.0000E+00 6.7794E-01

8.2500E+00 6.5157E+00

8.5000E+00 1.3032E+01

8.7500E+00 2.0256E+01

9.0000E+00 2.8215E+01

```

9.2500E+00  3.6939E+01
9.5000E+00  4.6454E+01
9.7500E+00  5.6790E+01
1.0000E+01  6.7975E+01
1.0250E+01  8.0037E+01
1.0500E+01  9.3004E+01
1.0750E+01  1.0690E+02
1.1000E+01  1.2177E+02
1.1250E+01  1.3762E+02
1.1500E+01  1.5449E+02
1.1750E+01  1.7241E+02

```

```

LATTICE VIBRATION MODEL- ENTER INPT, IGRN, RV, TG, GAML
-1 4 - 1 -

```

```

ELECTRONIC TERM - ENTER ENTROPY FILE NAME OR OPTION
elefe

```

```

ENTER MATERIAL NUMBER AND FILE NAME FOR EOS TABLE
100 b100

```

```

OPTION?

```

```

! Make EOS table

```

```

slib sol

```

```

ENTER ID NUMBER FOR TABLE TYPE
301

```

```

DENSITY MESH - ENTER RMIN, RMAX, NPTS, MTYPE, TREF
7.0 7.8724 5 1

```

```

DENSITY MESH - ENTER RMIN, RMAX, NPTS, MTYPE, TREF
7.8724 8.85 11 1

```

```

DENSITY MESH - ENTER RMIN, RMAX, NPTS, MTYPE, TREF
8.85 13 11 1

```

```

DENSITY MESH - ENTER RMIN, RMAX, NPTS, MTYPE, TREF

```

```

TEMPERATURE MESH - ENTER TMIN, TMAX, NPTS, MTYPE, RREF
0 298 4 1

```

```

TEMPERATURE MESH - ENTER TMIN, TMAX, NPTS, MTYPE, RREF
1809 0 1 1

```

```

TEMPERATURE MESH - ENTER TMIN, TMAX, NPTS, MTYPE, RREF
298 3134 29 2

```

```

TEMPERATURE MESH - ENTER TMIN, TMAX, NPTS, MTYPE, RREF
800 1200 17 1

```

```

TEMPERATURE MESH - ENTER TMIN, TMAX, NPTS, MTYPE, RREF

```

```

MAKE MAXWELL CONSTRUCTIONS? (YES/NO)

```

```

-

```

```

ENTER ID NUMBER FOR TABLE TYPE

```

```

-

```

```

ENTER MATID, DATE, BINLIB, AND ASCLIB

```

```

101 011993 balp aalp

```

```

OPTION?

```

```

! Make EOS table - high temperature section

```

```

mod sol wsl=1.42

```

```

OPTION?

```

```

slib sol

```

```

ENTER ID NUMBER FOR TABLE TYPE
301

```

Multiphase Iron EOS

```
MAKE MAXWELL CONSTRUCTIONS? (YES/NO)
-
ENTER ID NUMBER FOR TABLE TYPE
-
ENTER MATID, DATE, BINLIB, AND ASCLIB
101 011893 balpx aalpx
OPTION?
reset
OPTION?
!*****
!
! File dated 01/18/93 - Equation of state for gamma-phase iron.
! Tabular cold curve is Birch-Murnaghan form, with R0=8.060, B0=174.0,
! B0P=4.70. Thermal electronic term is included.
! The energy zero is set to zero density and temperature.
!
!*****
! Setup
sym eb=7.337 seb=-7.337 ro=8.06 bo=174 gam=1.65 deb=300
OPTION?
!
mod sol crv=1 nuc=1 tel=1 esft=seb
SOLID-LIQUID MODEL - ENTER MOLECULAR FORMULA
fe
    MOLES = 1.0000E+00, Z = 2.6000E+01, AW = 5.5847E+01
    FZ = 2.6000E+01, FW = 5.5847E+01, ZAV = 2.6000E+01
ENTER ECOH, RHOREF, TREF, GAMREF, DEBREF, CB, PSSN
7.285 7.9534 298 gam deb
COLD CURVE - ENTER ICLD, RTFD, RLJ, FACLJ
4 11 7.0 1
ENTER NAME OF INPUT FILE
tty
ENTER DENSITY AND PRESSURE, POINT BY POINT
6.5000E+00 -2.2655E+01
6.7500E+00 -2.0390E+01
7.0000E+00 -1.7640E+01
7.2500E+00 -1.4380E+01
7.5000E+00 -1.0583E+01
7.7500E+00 -6.2242E+00
8.0000E+00 -1.2775E+00
8.2500E+00 4.2825E+00
8.5000E+00 1.0481E+01
8.7500E+00 1.7344E+01
9.0000E+00 2.4897E+01
9.2500E+00 3.3164E+01
9.5000E+00 4.2172E+01
9.7500E+00 5.1945E+01
1.0000E+01 6.2509E+01
1.0250E+01 7.3889E+01
1.0500E+01 8.6111E+01
1.0750E+01 9.9199E+01
1.1000E+01 1.1318E+02
1.1250E+01 1.2807E+02
1.1500E+01 1.4391E+02
```

1.1750E+01 1.6072E+02

LATTICE VIBRATION MODEL- ENTER INPT, IGRN, RV, TG, GAML

-1 4 - 1 -

ELECTRONIC TERM - ENTER ENTROPY FILE NAME OR OPTION

elefe

OPTION?

! Make EOS table

slib sol

ENTER ID NUMBER FOR TABLE TYPE

301

DENSITY MESH - ENTER RMIN, RMAX, NPTS, MTYPE, TREF

7.0 7.8724 5 1

DENSITY MESH - ENTER RMIN, RMAX, NPTS, MTYPE, TREF

7.8724 8.85 11 1

DENSITY MESH - ENTER RMIN, RMAX, NPTS, MTYPE, TREF

8.85 13 11 1

DENSITY MESH - ENTER RMIN, RMAX, NPTS, MTYPE, TREF

13 18.5 8 3 298

DENSITY MESH - ENTER RMIN, RMAX, NPTS, MTYPE, TREF

18.5 98 9 3 298

DENSITY MESH - ENTER RMIN, RMAX, NPTS, MTYPE, TREF

1.e3 0 1 1

DENSITY MESH - ENTER RMIN, RMAX, NPTS, MTYPE, TREF

TEMPERATURE MESH - ENTER TMIN, TMAX, NPTS, MTYPE, RREF

0 298 4 1

TEMPERATURE MESH - ENTER TMIN, TMAX, NPTS, MTYPE, RREF

1809 0 1 1

TEMPERATURE MESH - ENTER TMIN, TMAX, NPTS, MTYPE, RREF

298 3134 29 2

TEMPERATURE MESH - ENTER TMIN, TMAX, NPTS, MTYPE, RREF

3135 6000 9 2

TEMPERATURE MESH - ENTER TMIN, TMAX, NPTS, MTYPE, RREF

6000 2.5e4 12 2

TEMPERATURE MESH - ENTER TMIN, TMAX, NPTS, MTYPE, RREF

2.5e4 1.e5 10 2

TEMPERATURE MESH - ENTER TMIN, TMAX, NPTS, MTYPE, RREF

1.e5 1.2e7 9 2

TEMPERATURE MESH - ENTER TMIN, TMAX, NPTS, MTYPE, RREF

MAKE MAXWELL CONSTRUCTIONS? (YES/NO)

-

ENTER ID NUMBER FOR TABLE TYPE

-

ENTER MATID, DATE, BINLIB, AND ASCLIB

102 011893 bgam agam

OPTION?

reset

OPTION?

!*****

!

! File dated 01/18/93 - Equation of state for epsilon-phase iron.

! Tabular cold curve is Birch-Murnaghan fit to static data, with

Multiphase Iron EOS

```

! R0=8.430, B0=184.0, B0P=5.0. Thermal electronic term is included.
! Energy zero is set to zero density and temperature.
!
!*****
! Setup
sym eb=7.394 seb=-7.394 ro=8.430 bo=182 gam=2.40 deb=385
OPTION?
!
mod sol crv=1 nuc=1 tel=1 esft=seb
SOLID-LIQUID MODEL - ENTER MOLECULAR FORMULA
fe
    MOLES = 1.0000E+00, Z = 2.6000E+01, AW = 5.5847E+01
    FZ = 2.6000E+01, FW = 5.5847E+01, ZAV = 2.6000E+01
ENTER ECOH,RHOREF,TREF,GAMREF,DEBREF,CB,PSSN
7.330 8.264 298 gam deb
COLD CURVE - ENTER ICLD,RTFD,RLJ,FACLJ
4 11 7.5 1
ENTER NAME OF INPUT FILE
tty
ENTER DENSITY AND PRESSURE, POINT BY POINT
7.0000E+00 -2.1536E+01
7.2500E+00 -1.9058E+01
7.5000E+00 -1.6071E+01
7.7500E+00 -1.2546E+01
8.0000E+00 -8.4529E+00
8.2500E+00 -3.7629E+00
8.5000E+00 1.5534E+00
8.7500E+00 7.5251E+00
9.0000E+00 1.4182E+01
9.2500E+00 2.1553E+01
9.5000E+00 2.9667E+01
9.7500E+00 3.8555E+01
1.0000E+01 4.8246E+01
1.0250E+01 5.8769E+01
1.0500E+01 7.0154E+01
1.0750E+01 8.2430E+01
1.1000E+01 9.5628E+01
1.1250E+01 1.0978E+02
1.1500E+01 1.2491E+02
1.1750E+01 1.4105E+02

LATTICE VIBRATION MODEL- ENTER INPT,IGRN,RV,TG,GAML
-1 4 - 2 -
ELECTRONIC TERM - ENTER ENTROPY FILE NAME OR OPTION
elefe
OPTION?
! Make EOS table
slib sol
ENTER ID NUMBER FOR TABLE TYPE
301
DENSITY MESH - ENTER RMIN,RMAX,NPTS,MTYPE,TREF
7.8724 8.85 11 1
DENSITY MESH - ENTER RMIN,RMAX,NPTS,MTYPE,TREF
8.85 13 11 3 298

```



```

DENSITY MESH - ENTER RMIN,RMAX,NPTS,MTYPE,TREF
13 18.5 8 3 298
DENSITY MESH - ENTER RMIN,RMAX,NPTS,MTYPE,TREF
18.5 98 9 3 298
DENSITY MESH - ENTER RMIN,RMAX,NPTS,MTYPE,TREF
1.e3 0 1 1
DENSITY MESH - ENTER RMIN,RMAX,NPTS,MTYPE,TREF

TEMPERATURE MESH - ENTER TMIN,TMAX,NPTS,MTYPE,RREF
0 298 4 1
TEMPERATURE MESH - ENTER TMIN,TMAX,NPTS,MTYPE,RREF
1809 0 1 1
TEMPERATURE MESH - ENTER TMIN,TMAX,NPTS,MTYPE,RREF
298 3134 29 2
TEMPERATURE MESH - ENTER TMIN,TMAX,NPTS,MTYPE,RREF
3135 6000 9 2
TEMPERATURE MESH - ENTER TMIN,TMAX,NPTS,MTYPE,RREF
6000 2.5e4 12 2
TEMPERATURE MESH - ENTER TMIN,TMAX,NPTS,MTYPE,RREF

MAKE MAXWELL CONSTRUCTIONS? (YES/NO)
-
ENTER ID NUMBER FOR TABLE TYPE
-
ENTER MATID, DATE, BINLIB, AND ASCLIB
103 011893 beps aeps
OPTION?
reset
OPTION?
!*****
!
! File dated 01/18/93 - Equation of state for liquid iron.
! Cold curve parameters are the same as those for the epsilon phase.
! The thermal electronic term is included.
! The energy zero is set to zero density and temperature.
!
!*****
! Setup
sym eb=7.397 seb=-7.397 ro=8.430 bo=182 gam=2.40 deb=385
OPTION?
!
mod sol crv=1 nuc=1 tel=1 esft=seb
SOLID-LIQUID MODEL - ENTER MOLECULAR FORMULA
fe
    MOLES = 1.0000E+00, Z = 2.6000E+01, AW = 5.5847E+01
    FZ = 2.6000E+01, FW = 5.5847E+01, ZAV = 2.6000E+01
ENTER ECOH,RHOREF,TREF,GAMREF,DEBREF,CB,PSSN
7.330 8.264 298 gam deb
COLD CURVE - ENTER ICLD,RTFD,RLJ,FACLJ
4 11 7.5 .68
ENTER NAME OF INPUT FILE
tty
ENTER DENSITY AND PRESSURE, POINT BY POINT
7.0000E+00 -2.1536E+01

```

Multiphase Iron EOS

```

7.2500E+00 -1.9058E+01
7.5000E+00 -1.6071E+01
7.7500E+00 -1.2546E+01
8.0000E+00 -8.4529E+00
8.2500E+00 -3.7629E+00
8.5000E+00 1.5534E+00
8.7500E+00 7.5251E+00
9.0000E+00 1.4182E+01
9.2500E+00 2.1553E+01
9.5000E+00 2.9667E+01
9.7500E+00 3.8555E+01
1.0000E+01 4.8246E+01
1.0250E+01 5.8769E+01
1.0500E+01 7.0154E+01
1.0750E+01 8.2430E+01
1.1000E+01 9.5628E+01
1.1250E+01 1.0978E+02
1.1500E+01 1.2491E+02
1.1750E+01 1.4105E+02

```

LATTICE VIBRATION MODEL- ENTER INPT, IGRN, RV, TG, GAML

1 4 - 2 -

ELECTRONIC TERM - ENTER ENTROPY FILE NAME OR OPTION

elefe

OPTION?

mod liq crs=1 tel=1 esft=seb

CRIS MODEL - ENTER BEXP, EFAC, QFAC, TMIN, NGS, NZI, EPS, DR, DT, XG, WX1, WX2

0 .23 1 - - - - - 2.1 2.1

BFAC, BEXP, EFAC, QFAC = 7.707E+00 7.707E+00 2.300E-01 1.000E+00

TMIN, RFAC, NGS, NZI = 1.023E+03 2.057E-01 1000 1

EPS, DR, DT, XG = 1.000E-05 1.000E-02 1.000E-02 4.000E-01

WX1, WX2 = 2.100E+00 2.100E+00

OPTION?

! Make mesh for EOS table. Note - omit zero density point

! and temperatures below 1000K when making liquid table.

mesh sol

DENSITY MESH - ENTER RMIN, RMAX, NPTS, MTYPE, TREF

1.e-6 1.e-4 7 2

DENSITY MESH - ENTER RMIN, RMAX, NPTS, MTYPE, TREF

1.e-4 2.0 21 2

DENSITY MESH - ENTER RMIN, RMAX, NPTS, MTYPE, TREF

2.0 5.0 16 1

DENSITY MESH - ENTER RMIN, RMAX, NPTS, MTYPE, TREF

5.0 7.8724 12 1

DENSITY MESH - ENTER RMIN, RMAX, NPTS, MTYPE, TREF

7.8724 8.85 11 1

DENSITY MESH - ENTER RMIN, RMAX, NPTS, MTYPE, TREF

8.85 13 11 3 298

DENSITY MESH - ENTER RMIN, RMAX, NPTS, MTYPE, TREF

13 18.5 8 3 298

DENSITY MESH - ENTER RMIN, RMAX, NPTS, MTYPE, TREF

18.5 98 9 3 298

DENSITY MESH - ENTER RMIN, RMAX, NPTS, MTYPE, TREF

1.e3 0 1 1

```

DENSITY MESH - ENTER RMIN,RMAX,NPTS,MTYPE,TREF

TEMPERATURE MESH - ENTER TMIN,TMAX,NPTS,MTYPE,RREF
1809 0 1 1
TEMPERATURE MESH - ENTER TMIN,TMAX,NPTS,MTYPE,RREF
1051.1228 3134 15 2
TEMPERATURE MESH - ENTER TMIN,TMAX,NPTS,MTYPE,RREF
3135 6000 9 2
TEMPERATURE MESH - ENTER TMIN,TMAX,NPTS,MTYPE,RREF
6000 2.5e4 12 2
TEMPERATURE MESH - ENTER TMIN,TMAX,NPTS,MTYPE,RREF
2.5e4 1.e5 10 2
TEMPERATURE MESH - ENTER TMIN,TMAX,NPTS,MTYPE,RREF
1.e5 1.2e7 9 2
TEMPERATURE MESH - ENTER TMIN,TMAX,NPTS,MTYPE,RREF

OPTION?
save mesh mslig
OPTION?
! Make EOS table
slib liq
ENTER ID NUMBER FOR TABLE TYPE
301
MAKE MAXWELL CONSTRUCTIONS? (YES/NO)
no
ENTER ID NUMBER FOR TABLE TYPE
-
ENTER MATID, DATE, BINLIB, AND ASCLIB
104 011893 bliq aliq
OPTION?
reset
OPTION?
!*****
!
! File dated 01/19/93 - Multiphase equation of state for iron.
! The energy zero of the individual tables are set to zero density
! and temperature. The energy zero of the multiphase EOS is set to
! room temperature and zero pressure for the alpha phase.
!
!*****
mod trn
ENTER PHASE SEARCH PARAMETERS - RREF,RCRT,TCRT,PCPS,NCPS,ERR

ENTER MATERIAL NUMBER, FILE NAME, AND ENERGY SHIFT
101 balp 7.3163
ENTER MATERIAL NUMBER, FILE NAME, AND ENERGY SHIFT
101 balpx 7.3924
ENTER MATERIAL NUMBER, FILE NAME, AND ENERGY SHIFT
102 bgam 7.3217 ! shifted by .0054
ENTER MATERIAL NUMBER, FILE NAME, AND ENERGY SHIFT
103 beps 7.3313 ! shifted by .015 (match shock data)
ENTER MATERIAL NUMBER, FILE NAME, AND ENERGY SHIFT
104 bliq 7.3074 ! shifted by -.0089
ENTER MATERIAL NUMBER, FILE NAME, AND ENERGY SHIFT

```

Multiphase Iron EOS

```
5 PHASES SUCCESSFULLY LOADED FOR MODEL
OPTION?
! Make mesh for EOS table
mesh trn
DENSITY MESH - ENTER RMIN,RMAX,NPTS,MTYPE,TREF
0 0 1 1
DENSITY MESH - ENTER RMIN,RMAX,NPTS,MTYPE,TREF
1.e-6 1.e-4 7 2
DENSITY MESH - ENTER RMIN,RMAX,NPTS,MTYPE,TREF
1.e-4 2.0 21 2
DENSITY MESH - ENTER RMIN,RMAX,NPTS,MTYPE,TREF
2.0 5.0 16 1
DENSITY MESH - ENTER RMIN,RMAX,NPTS,MTYPE,TREF
5.0 7.8724 12 1
DENSITY MESH - ENTER RMIN,RMAX,NPTS,MTYPE,TREF
8.409 0 1 1 ! - density at 13.0 GPa transition point
DENSITY MESH - ENTER RMIN,RMAX,NPTS,MTYPE,TREF
7.8724 8.85 10 1
DENSITY MESH - ENTER RMIN,RMAX,NPTS,MTYPE,TREF
8.85 13 11 3 298
DENSITY MESH - ENTER RMIN,RMAX,NPTS,MTYPE,TREF
13 18.5 8 3 298
DENSITY MESH - ENTER RMIN,RMAX,NPTS,MTYPE,TREF
18.5 98 9 3 298
DENSITY MESH - ENTER RMIN,RMAX,NPTS,MTYPE,TREF
1.e3 0 1 1
DENSITY MESH - ENTER RMIN,RMAX,NPTS,MTYPE,TREF

TEMPERATURE MESH - ENTER TMIN,TMAX,NPTS,MTYPE,RREF
0 298 4 1
TEMPERATURE MESH - ENTER TMIN,TMAX,NPTS,MTYPE,RREF
1809 0 1 1
TEMPERATURE MESH - ENTER TMIN,TMAX,NPTS,MTYPE,RREF
298 3134 29 2
TEMPERATURE MESH - ENTER TMIN,TMAX,NPTS,MTYPE,RREF
3135 6000 9 2
TEMPERATURE MESH - ENTER TMIN,TMAX,NPTS,MTYPE,RREF
6000 2.5e4 12 2
TEMPERATURE MESH - ENTER TMIN,TMAX,NPTS,MTYPE,RREF
2.5e4 1.e5 10 2
TEMPERATURE MESH - ENTER TMIN,TMAX,NPTS,MTYPE,RREF
1.e5 1.2e7 9 2
TEMPERATURE MESH - ENTER TMIN,TMAX,NPTS,MTYPE,RREF

OPTION?
save mesh mstrn
OPTION?
! Make multiphase EOS table
slib trn
ENTER ID NUMBER FOR TABLE TYPE
201
ENTER FZ, FW, PREF, TREF, AND GUESS FOR RHOREF
26.0 55.847 0 298 7.87
```

```

COMPUTED STANDARD STATE - RHOREF, BREF = 7.87238E+00 1.63939E+02
ENTER ID NUMBER FOR TABLE TYPE
301
MAKE MAXWELL CONSTRUCTIONS? (YES/NO)
yes
ENTER TSPALL AND GUESS OF RSPALL
3134 5.15
      T(K)      RV(G/CC)      RL(G/CC)      PV(GPA)      PL(GPA)
ENTER TMIN, TMAX, AND GUESSES FOR RLO AND RUP
3135 2.3e4 2.e-4 5.15
  3.1350E+03  1.7704E-04  5.2024E+00  8.2574E-05  8.3432E-05
  3.4000E+03  4.2890E-04  4.8012E+00  2.1677E-04  2.1788E-04
  3.6874E+03  9.3858E-04  4.5502E+00  5.1364E-04  5.1358E-04
  3.9990E+03  1.8828E-03  4.2946E+00  1.1145E-03  1.1145E-03
  4.3370E+03  3.5066E-03  4.0961E+00  2.2416E-03  2.2413E-03
  4.7036E+03  6.2102E-03  3.9543E+00  4.2783E-03  4.2778E-03
  5.1012E+03  1.0481E-02  3.8390E+00  7.7506E-03  7.7506E-03
  5.5324E+03  1.6957E-02  3.7368E+00  1.3422E-02  1.3421E-02
  6.0000E+03  2.6514E-02  3.6398E+00  2.2347E-02  2.2349E-02
  6.8312E+03  5.2067E-02  3.4685E+00  4.7766E-02  4.7766E-02
  7.7775E+03  9.6267E-02  3.3427E+00  9.4979E-02  9.4979E-02
  8.8549E+03  1.5956E-01  3.2604E+00  1.7620E-01  1.7620E-01
  1.0082E+04  2.4066E-01  3.1708E+00  3.0946E-01  3.0946E-01
  1.1478E+04  3.3520E-01  3.0717E+00  5.1371E-01  5.1371E-01
  1.3068E+04  4.4761E-01  2.9550E+00  8.1560E-01  8.1560E-01
  1.4879E+04  6.0018E-01  2.7870E+00  1.2584E+00  1.2584E+00
  1.6940E+04  7.6153E-01  2.5052E+00  1.8462E+00  1.8462E+00
  1.9286E+04  9.6686E-01  2.3937E+00  2.6863E+00  2.6863E+00
  2.1958E+04  1.1958E+00  2.2879E+00  3.8009E+00  3.8009E+00
ENTER TMIN, TMAX, AND GUESSES FOR RLO AND RUP
-
ENTER ID NUMBER FOR TABLE TYPE
-
ENTER MATID, DATE, BINLIB, AND ASCLIB
2150 011993 b2150 a2150
OPTION?
end

```

Distribution

External Distribution

Stanley Klein, M2/321
The Aerospace Corp.
PO Box 92957
Los Angeles, CA 90009-2957

G. R. Johnson
Alliant Techsystems Inc.
7225 Northland Dr.
Brooklyn Park, MN 55428

Eric Peterson
MN11-2720
Alliant Techsystems, Inc.
600 Second St., NE
Hopkins, MN 55343

M. Alme
Alme and Associates
102 Stevens Forest Professional Center
9650 Santiago Road
Columbia, MD 21045

J. Walker
Amparo Corporation
P. O. Box 2687
Santa Fe, NM 87504

Frank Maestas
Principal Engineer
Applied Research Associates
4300 San Mateo Blvd.
Suite A220
Albuquerque, NM 87110

Richard Zernow
Applied Research Associates
714 West Jefferson Ave.
Suite 305
Lakewood, CO 80235

Howard Chung
Argonne National Laboratory
RE/331
9700 South Cass Avenue
Argonne, IL 60439-4817

Ernest L. Baker
Bldg 3022, SMCAR-AEE-WW
U. S. Army ARDEC
Picatinny Arsenal, NJ 07806-5000

Kent Kimsey (4)
U.S. Army Research Laboratory
AMSRL-WT-TC
Aberdeen Proving Ground, MD 21005-5066
Attn: G. Hauver, K. Kimsey, M. Raftenberg, J. Zukas

John Tipton
U. S. Army Engineer Division
HNDED-SY
PO Box 1600
Huntsville, AL 35807

R. Rohani
U.S. Army Engineer Waterways Experiment Station
Attn: CEWES-SD
3909 Halls Ferry Road
Vicksburg, MS 39180-6199

Shun-chin Chou
Army Materials Technology Laboratory
SLCMT-MRD
Watertown, MA 02172-0001

George Snyder
U. S. Army Missile Command
AMSMI-RD-ST-WF
Redstone, Arsenal, AL 35898-5247

David Tenenbaum
U. S. Army Tank Automotive Command
RD&E Center
Survivability Division
Mail Code MASTA-RSS
Warren, MI 48397-5000

Doug Everhart
Battelle Memorial Institute
505 King Ave.
Columbus, OH 43201-2693

Multiphase Iron EOS

Glen Salo
BDM Corporation
1801 Randolph Road SE
Albuquerque, NM 87106

Richard Beyer
Bettis Atomic Power Laboratory
Westinghouse Electric Company
Box 79
West Mifflin, PA 15122-0079

Steven Bishop
Belvoir RD&E Center
STRBE-NAA
Fort Belvoir, VA 22060-560

Kevin Housen (2), MS 87-60
The Boeing Company
PO Box 3999
Seattle, WA 98124
Attn: K. Housen , R. Schmidt

T. J. Ahrens
Seismological Laboratory
Division of Geological and Planetary Sciences
California Institute of Technology
Pasadena, CA 91125

S. Schuster
California Research & Technology
20943 Devonshire St.
Chatsworth, CA 94588

Dennis L. Orphal
California Research & Technology, Inc.
5117 Johnson Dr.
Pleasanton, CA 94588

Mark Majerus
California Research and Technology, Inc.
PO Box 2229
Princeton, NJ 08543-2229

Mark Smith
Aerophysics Branch
Calspan Corporation/AEDC Operations
MS 440
Arnold AFB, TN 37389

G. Lyles
CIA
6219 Lavell Ct.
Springfield VA 22152

John Walton
OSWR
CIA
Washington, DC 20505

N. W. Ashcroft
Laboratory of Atomic and Solid State Physics
Clark Hall
Cornell University
Ithaca, NY 14853

Carlos Marino
Industry, Science, and Technology Department
Cray Research Park
655 E. Lone Oak Dr.
Eagan, MN 55121

Stanley Willner
David Taylor Research Center
Mail Code 3510
Bethesda, MD 20084

Major Robert Kocher
Defense Advanced Research Projects Agency
3701 North Fairfax Drive
Arlington, VA 22203-1714

Michael E. Giltrud
DNA/SPSD
6801 Telegraph Rd.
Alexandria, VA 22310

Randy Hanson
Denver Research Institute
University Park
Denver, CO 80208

Brian Scott
EI Dupont de Demours and Company
Chestnut Run - CR702
Wilmington, DL 19898

Multiphase Iron EOS

William Flis
DynaEast Corporation
3201 Arch Street
Philadelphia, PA 19104

Randall Laviolette
EG&G Idaho
P.O. Box 1625
Idaho Falls, ID 83415-2208

Tien Chou
EG&G Mound
PO Box 3000
Miamisburg, OH 45343

Julius W. Enig
Enig Associates, Inc.
11120 New Hampshire Ave., Suite 500
Silver Spring, MD 20904-2633

Kim Parnell
Failure Analysis Associates, Inc.
149 Commonwealth Ave.
P. O. Box 3015
Menlo Park, CA 94025

Vensen Wu
FMC Corporation
MS-P95
2890 De La Cruz Blvd.
Santa Clara, CA 95052

Kenneth Lockwood
Knolls Atomic Power Laboratory
General Electric Company
PO Box 1072
Schenectady, NY 12301-1072

James MacDonald
General Research Corporation
PO Box 6770
Santa Barbara, CA 93160-6770

Guy Spitale
Jet Propulsion Laboratory
California Institute of Technology
Reliability Engineering Section
4800 Oak Grove Drive
Pasadena, CA 91109

Jeff Elder
Kaman Sciences Corporation
Huntsville Office
P. O. Box 2486
Huntsville, AL 35804-2486

John May
Kaman Sciences Corporation
1500 Garden of the Gods Road
Colorado Springs, CO 80933

Thomas Grondzik
Kendall Square Research
2102 Business Center Drive, Suite 115D
Irvine, CA 92715

E. S. Gaffney
Ktech Corporation
911E Pennsylvania NE
Albuquerque, NM 87112

Ed Cykowski
Lockheed Engineering and Space Company
Mail Code B22
2400 NASA Road 1
Houston, TX 77058-3711

Erik Matheson (2)
O/81-12 B/157
Lockheed Missiles & Space Company
1111 Lockheed Way
Sunnyvale, CA 94088-3504
Attn: Y.-I. Choo, E. Matheson

Richard Crawford
Logicon RDA
P. O. Box 92500
Los Angeles, CA 90009

John Flowers
LTV Missiles and Electronics Group
P. O. Box 650003
M/S EM-36
Dallas, TX 75265-0003

Tim Gillespie
MS H4330
Martin Marietta Astronautics Group
PO Box 179
Denver, CO 80201

Multiphase Iron EOS

George Christoph
Martin Marietta Laboratories
1450 S. Rolling Road
Baltimore, Maryland 21227

Larry Williams
Martin Marietta
MP 126
Box 5837
Orlando, FL 32855

N. A. Louie
Department Y831, Mail Station 13-3
McDonnell Douglas Missile Space Systems Company
5301 Bolsa Avenue
Huntington Beach, CA 92647

Eric Christiansen
NASA Johnson Space Center
Space Science Branch/SN3
Houston, TX 77058

Scott Hill
NASA Marshall Space Flight Center
Mail Code ED52
Redstone Arsenal
Huntsville, AL 35812

John M. Pipkin (Code 4310)
Naval Coastal Systems Center
Thomas Drive
Panama City Beach, FL 32405-5000

D. G. Tasker, R13
Naval Surface Warfare Center
Dahlgren, VA 22448-5000

Hans Mair
Naval Surface Warfare Center
10901 New Hampshire Ave.
Silver Spring, MD 20903-5000

Phil Miller, R-13 (2)
Naval Surface Warfare Center
10901 New Hampshire Ave.
Silver Spring, MD 20903-5000
Attn: J. Forbes, P. Miller

Dan Bowlus
Naval Underwater Systems Center
Mail Code 8123
Newport, RI 02841-5047

Eric Lundstrom
Code 3261
Naval Weapons Center
China Lake, CA 93555

P.-A. Persson
CETR
New Mexico Tech
Socorro, NM 87801

Mark Walz
NMI
2229 Main Street
Concord, MA 01742

Dr. Yasuyuki Horie
Box 7908
North Carolina State University
Raleigh, NC 27695

Firooz Allahdadi (3)
Phillips Laboratory
PL/WSSD
Kirtland AFB, NM 87117-6008
Attn: F. Allahdadi, D. Fulk, D. Medina

Ray Pierce
Physics International
PO Box 5010
San Leandro, CA 94577-0599

Keith Pauley
PNL
KS-42
P. O. Box 999
Richland, WA 99352

Steve Rieco
POD Associates, Inc.
2309 Renard Place, SE
Suite 201
Albuquerque, NM 87106

Multiphase Iron EOS

C. W. Nestor, Jr.
Oak Ridge National Laboratory
PO Box 2009
Oak Ridge, TN 37831-8058

Anthony Gurule
Orion International Inc.
Suite 200
300 San Mateo NE
Albuquerque, NM 87108

D. Matuska
Orlando Technology, Inc.
P. O. Box 855
Shalimar, FL 32579

John Remo
Quantametrics, Inc.
#1 Brackenwood Path
Head of the Harbor
St. James, NY 11780

Peter Radkowski, III
Radkowski Associates
PO Box 1121
Los Alamos, NM 87544

D. Labreche
Re/Spec, Inc., Suite 300
4775 Indian School Rd. NE
Albuquerque, NM 87110

Greg L. Savoni
Rockwell International Corporation
12214 Lakewood Blvd.
NA-40
Downey, CA 90241

R&D Associates
6053 West Century Boulevard
P.O. Box 92500
Los Angeles, CA 90009
Attn: B. Lee

Mark Fry
SAIC/New York
8 West 40th Street
14 Floor
New York, New York 10018

Ronald Weitz
SAIC
2109 Air Park Road SE
Albuquerque, NM 87106

James Zerkle
SAIC
Suite A
11696 Sorrento Valley Road
San Diego, CA 92121

Charles E. Needham
Maxwell/S-CUBED
2501 Yale SE
Suite 300
Albuquerque, NM 87106

Steve Peyton
S-CUBED
P. O. Box 1620
LaJolla, CA 92038-1620

C. E. Anderson (2)
Southwest Research Institute
P.O. Drawer 28510
San Antonio, TX 78284
Attn.: C. E. Anderson, J. D. Walker

William G. Tanner
Space Science Laboratory
P. O. Box 97303
Waco, TX 76798

L. Seaman
SRI International
333 Ravenswood Ave.
Menlo Park, CA 94025

Bhuminder Singh
Teledyne Brown Engineering
Cummings Research Park
300 Sparkman Dr., NW
PO Box 070007
Huntsville, AL 35807-7007

Steve Herrick
Textron Defense Systems
Mail Stop 1115
201 Lowell St.
Wilmington, MA 01887

Multiphase Iron EOS

Dwight Clark, Mailstop 280
Thiokol Corporation
Advanced Technology Division
P. O. Box 707
Brigham City, Utah 84302

Akhilesh Maewal
Trans-Science Corporation
7777 Fay Avenue
Suite 112
La Jolla, CA 92037

Stan Fink, R1/1044
TRW
One Space Park
Redondo Beach, CA 90278

T. P. Shivananda
TRW Ballistic Missiles Group
SB/2/1011
P. O. Box 1310
San Bernardino, CA 92402-1310

Brent Webb
Umpqua Research Company
P. O. Box 791
125 Volunteer Way
Myrtle Creek, OR 97457

Gene Carden
University of Alabama
PO Box 870278
Tuscaloosa, AL 35487-0278

Gary Hough
Aerophysics Research Facility
University of Alabama at Huntsville
Huntsville, AL 35899

R. Jeanloz
Department of Geology and Geophysics
University of California
Berkeley, CA 94720

David J. Benson
Dept. of AMES R-011
University of California San Diego
La Jolla, CA 92093

Robert Culp
Department of Aerospace Engineering Sciences
Campus Box 429
University of Colorado
Boulder, CO 80309

Garry Abfalter
Impact Physics Group
University of Dayton Research Institute
300 College Park, Room KLA 14
Dayton, OH 45469-0182

G. Ali Mansoori
Department of Energy Engineering
University of Illinois at Chicago Circle
Box 4348
Chicago, IL 60680

Chen-Chi Hsu
University of Florida
Department of Aerospace Engineering
231 Aerospace Building
Gainesville, FL 32611

Murli H. Manghnani
Hawaii Institute of Geophysics
University of Hawaii
Honolulu, Hawaii 96822

Scott Stewart
Department of Theoretical and Applied Mechanics
University of Illinois
Urbana, Illinois 61801

R. D. Dick
Department of Mechanical Engineering
University of Maryland
College Park, MD 20742

R. L. McCrory
Laboratory for Laser Energetics
University of Rochester
250 East River Road
Rochester, NY 14623-1299

H. M. Van Horn
Department of Physics and Astronomy
University of Rochester
Rochester, NY 14627

Multiphase Iron EOS

Thomas Moriaty
Department of Engineering Sciences and Mechanics
University of Tennessee
Knoxville, TN 37996-2030

Stephan J. Bless
The University of Texas at Austin
Institute for Advanced Technology
4030-2 W. Braker Lane, Suite 200
Austin, TX 78712

Eric Fahrenthold
Department of Mechanical Engineering
The University of Texas at Austin
Austin, TX 78712

Dr. Chadee Persad
Institute for Advanced Technology
The University of Texas at Austin
4030-2 W. Braker Ln.
Austin, TX 78759-5329

Keith Holsapple
Department of Aeronautics and Astronautics FS10
The University of Washington
Seattle, WA 98195

Y. M. Gupta
Department of Physics
Shock Dynamics Laboratory
Washington State University
Pullman, WA 99164-2814

John A. Collins
Wright Laboratory
WL/MNMW
Eglin AFB, FL 32542-5434

Dan Brubaker
Wright Laboratory
WL/MNSA
Eglin AFB, FL 32542-5434

A. Ng
Department of Physics
University of British Columbia
Vancouver, BC V6T 26A
CANADA

Atomic Weapons Establishment (2)
Attn: P. C. Thompson, B. D. Lambourn
Aldermaston, Reading, RG7 4PR
Berkshire
ENGLAND

V. Hohler
Ernst-Mach-Institut
Eckerstrasse 4
7800 Freiburg i.BR
GERMANY

F. Hensel
Fachbereich Physikalische Chemie
Philipps-Universitat Marburg
Hans-Meerwein-Strasse
D-3550 Marburg
GERMANY

Centre d'Etudes de Limeil-Valenton (2)
Attn: F. Perrot, M. Penicaud
B.P. 27
F-94190 Villeneuve St. Georges
FRANCE

Centre d'Etudes de Vaujours (2)
Attn: R. Chirat, J. Baute
B.P. 7
F-77181 Courtry
FRANCE

J.-P. Hansen
Ecole Normale Supérieure de Lyon
46, allée d'Italie
69364 Lyon Cedex 07
FRANCE

S. K. Sikka
High Pressure Physics Division
Bhabha Atomic Research Centre
Trombay, Bombay - 400 085
INDIA

Y. Rosenfeld
Nuclear Research Center - Negev
P.O. Box 9001
Beer Sheva
ISRAEL

Multiphase Iron EOS

Los Alamos National Laboratory (75)
Mail Station 5000
P.O. Box 1663
Los Alamos, NM 87545

Attn: J. Abdallah, MS-212
Attn: T. F. Adams, MS F663
Attn: B. I. Bennett, MS B221
Attn: S. T. Bennion, MS F663
Attn: W. Birchler, MS G787
Attn: P. J. Blewett, MS F663
Attn: M. W. Burkett, MS G787
Attn: E. J. Chapyak, MS F663
Attn: R. A. Clark, MS B257
Attn: G. E. Cort, MS G787
Attn: C. W. Cranfill, MS-B257
Attn: B. J. Daly, MS B216
Attn: W. C. Davis, MS-P952
Attn: T. N. Dey, MS-F665
Attn: J. K. Dienes, MS B216
Attn: H. Flaush, MS C936
Attn: C. A. Forest, MS-P952
Attn: R. P. Godwin, MS F663
Attn: F. Harlow, MS B216
Attn: W. B. Harvey, MS F663
Attn: B. L. Holian, MS J569
Attn: K. S. Holian, MS B295
Attn: J. W. Hopson, MS B216
Attn: H. Horak, MS C936
Attn: M. L. Hudson, MS J970
Attn: E. S. Idar, MS-J960
Attn: J. D. Johnson, MS-B267
Attn: J. N. Johnson, MS-B267
Attn: N. L. Johnson, MS B216
Attn: J. E. Kennedy, MS-B950
Attn: J. F. Kerrisk, MS G787
Attn: M. Klein, MS F669
Attn: D. Kothe, MS-B216
Attn: R. A. Krajcik, MS-F664
Attn: W. H. Lee, MS B226
Attn: R. A. Lesar, MS-B262
Attn: L. B. Luck, MS-K557
Attn: C. L. Mader, MS-B214
Attn: J. M. Mack, MS-P940
Attn: D. Mandell, MS F663
Attn: L. G. Margolin, MS D406
Attn: G. H. McCall, MS B218
Attn: J. K. Meier, MS G787
Attn: R. W. Meier, MS G787
Attn: A. L. Merts, MS-212

Attn: C. E. Morris, MS-J970
Attn: T. R. Neal, MS-P940
Attn: A. T. Oyer, MS G787
Attn: D. A. Poling, MS-F669
Attn: C. E. Ragan, MS-D449
Attn: J. Ramsay, MS-J960
Attn: M. Rich, MS F669
Attn: J. Richey, MS-B214
Attn: M. Sahota, MS B257
Attn: J. W. Shaner, MS-J970
Attn: D. H. Sharp, MS-B285
Attn: S. Shaw, MS-B214
Attn: W. Sparks, MS F663
Attn: G. K. Straub, MS-B267
Attn: P. K. Tang, MS-F664
Attn: M. T. Thieme, MS-F664
Attn: D. Tonks, MS B267
Attn: H. E. Trease, MS B257
Attn: J. D. Wackerle, MS-P952
Attn: L. Witt, MS C936

Multiphase Iron EOS

University of California (25)
Lawrence Livermore National Laboratory
7000 East Ave.
P.O. Box 808
Livermore, CA 94550

Attn: A. Attia, MS L-200
Attn: D. E. Burton, MS L-18
Attn: R. B. Christensen, MS L-35
Attn: G. R. Gathers, L368
Attn: H. C. Graboske, MS L-296
Attn: R. Grover, MS L-299
Attn: J. M. LeBlanc, MS L-35
Attn: E. L. Lee, MS L-368
Attn: D. A. Liberman, L477
Attn: A. K. McMahan, L299
Attn: W. Moran, MS L-200
Attn: R. M. More, MS L-321
Attn: M. J. Murphy, MS L-368
Attn: W. J. Nellis, MS L-299
Attn: A. L. Nichols, MS L-368
Attn: J. E. Reaugh, MS L-290
Attn: F. H. Ree, MS L-299
Attn: C. E. Rosenkilde, L84
Attn: M. Ross, MS L-299
Attn: D. J. Steinberg, MS L-35
Attn: C. M. Tarver, MS L-368
Attn: R. E. Tipton, MS L-35
Attn: M. van Thiel, MS L-299
Attn: M. Wilkins, MS L-321
Attn: D. A. Young, MS L-299

Sandia Internal

1020 W. Herrmann
1153 G. A. Samara
1153 R. A. Graham
1153 A. C. Switendick
1200 G. O. Allshouse
1241 M. A. Sweeney
1271 M. K. Matzen
1271 E. J. McGuire
1400 E. H. Barsis
1404 J. A. Ang
1425 J. H. Biffle
1431 J. M. McGlaun
1431 K. G. Budge
1431 D. Campbell
1431 M. G. Elrick
1431 E. S. Hertel
1431 R. J. Lawrence
1431 J. S. Peery
1431 S. V. Petney
1431 A. C. Robinson
1431 T. G. Trucano
1431 M. Wong
1431 L. Yarrington
1431 CTH Day File
1432 P. Yarrington
1432 R. L. Bell
1432 R. M. Brannon
1432 P. J. Chen
1432 H. E. Fang
1432 A. V. Farnsworth
1432 G. I. Kerley (10)
1432 M. E. Kipp
1432 F. R. Norwood
1432 S. A. Silling
1432 P. A. Taylor
1433 P. L. Stanton
1433 M. Boslough
1433 L. C. Chhabildas
1433 M. D. Furnish
1433 D. E. Grady
1434 D. Martinez
1503 L. W. Davison
1511 J. S. Rottler
1512 A. C. Ratzel
1512 M. R. Baer
1512 M. L. Hobbs
1513 R. D. Skocypec

Multiphase Iron EOS

1553 W. L. Hermina
1561 H. S. Morgan
1562 R. K. Thomas
2510 D. H. Anderson
2512 J. G. Harlan
2513 D. E. Mitchell
2514 L. L. Bonzon
5166 R. E. Setchell
5602 J. R. Asay
6111 J. L. Wise
6117 W. R. Wawersik
6418 S. L. Thompson
6418 L. N. Kmetyk
6515 M. Berman
6515 K. Boyack
8741 G. A. Benedetti
8741 M. L. Chiesa
8741 L. E. Voelker
8742 J. J. Dike
8243 M. L. Callabresi
8743 D. J. Bammann
8744 C. M. Hartwig
8745 R. J. Kee
9311 A. J. Chabai
9311 T. Bergstresser
9722 R. O. Nellums
9723 J. M. Holovka
9723 M. J. Forrestal
8523-2 Central Technical Files
7141 Technical Library (5)
7151 Technical Publications
7613-2 Document Processing for DOE/OSTI (10)